

Iron from coal combustion particles dissolves much faster than mineral dust under simulated atmospheric acid conditions

Clarissa Baldo¹, Akinori Ito², Michael D. Krom^{3,4}, Weijun Li⁵, Tim Jones⁶, Nick Drake⁷, Konstantin Ignatyev⁸, Nicholas Davidson¹, Zongbo Shi¹

¹School of Geography Earth and Environmental Sciences, University of Birmingham, Birmingham, United Kingdom

²Yokohama Institute for Earth Sciences, JAMSTEC, Yokohama, Kanagawa 236-0001, Japan

³Morris Kahn Marine Station, Charney School of Marine Sciences, University of Haifa, Haifa, Israel

⁴School of Earth and Environment, University of Leeds, Leeds, United Kingdom

⁵Department of Atmospheric Sciences, School of Earth Sciences, Zhejiang University, Hangzhou 310027, China

⁶School of Earth and Environmental Sciences, Cardiff University, Cardiff, United Kingdom

⁷Department of Geography, King's College London, London, United Kingdom

⁸Diamond Light Source, Didcot, Oxfordshire, United Kingdom

Correspondence to: Zongbo Shi (z.shi@bham.ac.uk); Akinori Ito (akinori@jamstec.go.jp)

Abstract. Mineral dust is the largest source of aerosol iron (Fe) to the offshore global ocean, but acidic processing of coal fly ash (CFA) in the atmosphere could be an important source of soluble aerosol Fe. Here, we determined the Fe speciation and dissolution kinetics of CFA from Aberthaw (United Kingdom), Krakow (Poland), and Shandong (China) in solutions which simulate atmospheric acidic processing. In CFA-PM₁₀ fractions, 8%-21.5% of the total Fe was as hematite and goethite (dithionite extracted Fe), 2%-6.5% as amorphous Fe (ascorbate extracted Fe), while magnetite (oxalate extracted Fe) varied from 3%-22%. The remaining 50%-87% of Fe was associated with other Fe-bearing phases, possibly aluminosilicates. High concentrations of ammonium sulfate ((NH₄)₂SO₄), often found in wet aerosols, increased Fe solubility of CFA up to 7 times at low pH (2-3). The oxalate effect on the Fe dissolution rates at pH 2 varied considerably depending on the samples, from no impact for Shandong ash to doubled dissolution for Krakow ash. However, this enhancement was suppressed in the presence of high concentrations of (NH₄)₂SO₄. Dissolution of highly reactive (amorphous) Fe was insufficient to explain the high Fe solubility at low pH in CFA, and the modelled dissolution kinetics suggest that other Fe-bearing phases such as magnetite may also dissolve relatively rapidly under acidic conditions. Overall, Fe in CFA dissolved up to 7 times faster than in a Saharan dust precursor sample at pH 2. Based on these laboratory data, we developed a new scheme for the proton- and oxalate-promoted Fe dissolution of CFA, which was implemented into the global atmospheric chemical transport model IMPACT. The revised model showed a better agreement with observations of Fe solubility in aerosol particles over the Bay of Bengal, due to the initial rapid release of Fe and the suppression of the oxalate-promoted dissolution at low pH. The improved model enabled us to predict sensitivity to a more dynamic range of pH changes, particularly between anthropogenic combustion and biomass burning aerosols.

33 **1 Introduction**

34 The availability of iron (Fe) limits primary productivity in high-nutrient low-chlorophyll (HNLC) regions of the global ocean
35 including the subarctic North Pacific, the East Equatorial Pacific and the Southern Ocean (Boyd et al., 2007; Martin, 1990). In
36 other regions of the global ocean such as the subtropical North Atlantic, the Fe input may affect primary productivity by
37 stimulating nitrogen fixation (Mills et al., 2004; Moore et al., 2006). These areas are particularly sensitive to changes in the
38 supply of bioavailable Fe. Atmospheric aerosols are an important source of soluble (and, thus potentially bio-accessible) Fe to
39 the offshore global ocean. The deposition of bio-accessible Fe to the ocean can alter biogeochemical cycles and increase the
40 carbon uptake, consequently affecting the climate (e.g., Jickells and Moore, 2015; Jickells et al., 2005; Kanakidou et al., 2018;
41 Mahowald et al., 2010; Shi et al., 2012). In general, bio-accessible Fe consists of aerosol dissolved Fe, and Fe-nanoparticles
42 which can be present in the original particulate matter and/or formed during atmospheric transport as a result of cycling into
43 and out of clouds (Shi et al., 2009). It is in addition possible that other more refractory forms of Fe could be solubilised in the
44 surface waters by zooplankton (Schlosser et al., 2018) or the microbial community (Rubin et al., 2011).

45 The Fe transported in the atmosphere is largely derived from lithogenic sources, which contribute around 95% of the total Fe
46 in suspended particles (e.g., Shelley et al., 2018) and most studies so far have concentrated on atmospheric processing of
47 mineral dust (e.g., Cwiertny et al., 2008; Fu et al., 2010; Ito and Shi, 2016; Shi et al., 2011a; Shi et al., 2015). Mineral dust has
48 low Fe solubility (dissolved Fe/ total Fe \times 100) near the source regions, generally below 1% (e.g., Shi et al., 2011c; Sholkovitz
49 et al., 2009; Sholkovitz et al., 2012), increasing somewhat as a result of processes occurring during atmospheric transport (e.g.,
50 Baker et al., 2021; Baker et al., 2020). Other sources of bio-accessible Fe to the ocean are from combustion sources such as
51 biomass burning, coal combustion, oil combustion, and metal smelting (e.g., Ito et al., 2018; Rathod et al., 2020). Although
52 these sources are only a small fraction of the total Fe in atmospheric particulates, the Fe solubility of pyrogenic sources can be
53 1–2 orders of magnitude higher than in mineral dust (Ito et al., 2021b and references therein), and thus can be important in
54 promoting carbon uptake. However the Fe solubility of pyrogenic sources varies considerably depending on the particular
55 sources, with higher values observed for oil combustion and biomass burning than coal combustion sources (Ito et al., 2021b
56 and references therein).

57 Wang et al. (2015) estimated that coal combustion emitted around ~ 0.9 Tg yr⁻¹ of Fe into the atmosphere (on average for 1960–
58 2007), contributing up to $\sim 86\%$ of the total anthropogenic Fe emissions. A more recent study, which has included metal
59 smelting as an atmospheric Fe source, estimated that coal combustion emitted ~ 0.7 Tg yr⁻¹ of Fe for the year 2010, contributing
60 around 34% of the total anthropogenic Fe atmospheric loading (Rathod et al., 2020). Although the use of coal as a principal
61 energy source has been recently reduced as a result of concern about air quality and global warming, coal is still an important
62 energy source in a number of countries in particular in the Asia-Pacific region (BP, 2020). In China, most of the total energy
63 is supplied by coal, contributing over 50% of the global coal consumption in 2019, followed by India (12%), and the US (8%).
64 Germany and Poland are the largest coal consumers in Europe, accounting together for around 40% of the European usage
65 (BP, 2020). South Africa is also among the principal countries for coal consumption (BP, 2020) and is a source of Fe-bearing
66 particles to the anaemic Southern Ocean (e.g., Ito et al., 2019).

67 Coal fly ash (CFA) is a by-product of coal combustion. This generally consists of glassy spherical particles (e.g., Brown et al.,
68 2011), which are formed through different transformations (decomposition, fusion, agglomeration, volatilization) of mineral
69 matter in coal during combustion (e.g., Jones, 1995), and are transported with the flue gases undergoing rapid solidification.
70 CFA are co-emitted with acidic gases such as sulfur dioxide (SO₂), nitrogen oxides (NO_x) and carbon dioxide (CO₂) (e.g.,
71 Munawar, 2018).

72 During long-range transport, CFA particles undergo atmospheric processing with the CFA surface coated by acidic species
73 such as sulfuric acid (H_2SO_4) and oxalic acid ($\text{H}_2\text{C}_2\text{O}_4$) in atmospheric aerosols. Aged CFA particles are hygroscopic and
74 absorb water at typical relative humidity in the marine atmosphere. As a result, a thin layer of water with high acidity, low pH
75 and high ionic strength is formed around the particles (Meskhidze et al., 2003; Spokes and Jickells, 1995; Zhu et al., 1992). In
76 addition, ammonia (NH_3) which is a highly hydrophilic gas, can also partition into the aerosol phase, react with H_2SO_4 and
77 form ammonium sulfate ($(\text{NH}_4)_2\text{SO}_4$) an important inorganic salt contributing to the high ionic strength in aged atmospheric
78 aerosols (Seinfeld and Pandis, 2016).

79 At low pH conditions, Fe solubility in aerosols increases, as the high concentration of protons (H^+) weakens the Fe-O bonds
80 facilitating the detachment of Fe from the surface lattice (Furrer and Stumm, 1986). Li et al. (2017) provided the first
81 observational evidence that acidification leads to the release of Fe from anthropogenic particles.

82 In addition to these inorganic processes, organic ligands can also enhance atmospheric Fe dissolution by forming soluble
83 complexes with Fe (e.g., Cornell and Schwertmann, 2003). For example, $\text{H}_2\text{C}_2\text{O}_4$ is an important organic species in aerosols
84 (e.g., Kawamura and Bikkina, 2016). Laboratory studies have demonstrated that $\text{H}_2\text{C}_2\text{O}_4$ increases Fe solubility of aerosol
85 sources (Chen and Grassian, 2013; Johnson and Meskhidze, 2013; Paris and Desboeufs, 2013; Paris et al., 2011; Xu and Gao,
86 2008). Recently, observations over the Bay of Bengal indicate that $\text{H}_2\text{C}_2\text{O}_4$ contributes to the increase of dissolved Fe in
87 atmospheric water (Bikkina et al., 2020).

88 To simulate the Fe dissolution in CFA, it is necessary to determine the dissolution kinetics under realistic conditions. Previous
89 studies have investigated the Fe dissolution kinetics of CFA under acidic conditions. Chen et al. (2012) simulated acidic and
90 cloud processing of certified CFA. Fu et al. (2012) determined the dissolution kinetics of CFA samples at pH 2, while Chen
91 and Grassian (2013) investigated the effect of organic species (e.g., oxalate and acetate) at pH 2-3. These studies showed that
92 high acidity and the presence of oxalate enhanced Fe dissolution at the surface of CFA particles, similar to those reported in
93 mineral dust (Chen et al., 2012; Chen and Grassian, 2013; Fu et al., 2012; Ito and Shi, 2016; Shi et al., 2011a). They also
94 demonstrated that there are large differences in dissolution rates in different types of CFA, likely related to Fe speciation.

95 Furthermore, high ionic strength, commonly seen in aerosol water, affects the activity of molecular species present in solution,
96 consequently it can significantly impact the Fe dissolution behaviour. Recent studies have considered the effect of the high
97 ionic strength on the Fe dissolution kinetics of CFA under acidic conditions. For example, the Fe solubility of CFA samples
98 was measured at pH 1-2 with high sodium chloride (NaCl) concentrations (Borgatta et al., 2016), and with high sodium nitrate
99 (NaNO_3) concentrations Kim et al. (2020). In real atmospheric conditions, NaCl or NaNO_3 are unlikely to be the main driver
100 of high ionic strength in aged CFA. Although NaCl can coagulate with dust particles in the marine boundary layer (Zhang et
101 al., 2003), the aging of CFA is primarily by the uptake of secondary species, particularly sulfate and ammonia (Li et al., 2003).
102 Ito and Shi (2016) found that at low pH and high concentration of $(\text{NH}_4)_2\text{SO}_4$ the Fe solubility of mineral dust is likely to be
103 enhanced by the adsorption of sulfate ions on the particle surface. However, to date the effect of high $(\text{NH}_4)_2\text{SO}_4$ concentrations
104 on the Fe dissolution behaviour in combustion sources in the presence or absence of oxalate remains unknown.

105 The dissolution kinetics measured by Chen and Grassian (2013) have been used to develop a modelled dissolution scheme for
106 CFA, assuming a single Fe-bearing phase in CFA (Ito, 2015). However, there are multiple Fe-bearing phases in CFA, primarily
107 hematite, magnetite and Fe in aluminium silicate glass (Brown et al., 2011; Chen et al., 2012; Fu et al., 2012; Kukier et al.,
108 2003; Kutchko and Kim, 2006; Lawson et al., 2020; Sutto, 2018; Valeev et al., 2019; Waanders et al., 2003; Wang, 2014;
109 Zhao et al., 2006), but also accessory Fe-bearing minerals for example silicates, carbonate, sulfides and sulfates (Zhao et al.,
110 2006). These phases have a range of reactivities. Previous studies showed that CFA dissolves much faster during the first 1-2

111 hours than subsequently (Borgatta et al., 2016; Chen et al., 2012; Chen and Grassian, 2013; Fu et al., 2012; Kim et al., 2020),
112 confirming the existence of multiple Fe-bearing phases within a single CFA sample with different dissolution behaviour.

113 In this study, laboratory experiments were conducted to determine the dissolution kinetics of coal combustion emission
114 products (i.e., CFA) during simulated atmospheric acidic processing in the presence of $(\text{NH}_4)_2\text{SO}_4$ and oxalate which are
115 commonly found in atmospheric aerosols. In particular, we investigated the effect of high $(\text{NH}_4)_2\text{SO}_4$ concentrations on the
116 proton-promoted and oxalate-promoted Fe dissolution at low pH conditions. Our study also determined the Fe-bearing phases
117 present in the CFA and compared them to those present in mineral dust. The experimental results enabled us to develop a new
118 Fe release scheme for CFA sources which was then implemented into the global atmospheric chemical transport model
119 IMPACT. The model results were compared with observations of Fe solubility in aerosol particles over the Bay of Bengal
120 from Bikkina et al. (2020).

121 **2 Materials and Methods**

122 **2.1 Sample collection and subsequent size fractionation**

123 CFA samples were collected from the electrostatic precipitators at three coal-fired power stations at different locations: United
124 Kingdom (Aberthaw ash), Poland (Krakow ash), and China (Shandong ash). The bulk samples were resuspended to obtain
125 aerosol fractions representative of particles emitted into the atmosphere. A custom-made resuspension system was used to
126 collect the PM_{10} fraction (particles with an aerodynamic diameter smaller than $10\ \mu\text{m}$), which is shown in Fig. S1. Around 20
127 g of sample was placed into a glass bottle and injected at regular intervals (2-5 sec) into a glass reactor ($\sim 70\ \text{L}$) by flushing the
128 bottle with pure nitrogen. The air in the reactor was pumped at a flow rate of $30\ \text{L}\ \text{min}^{-1}$ into a PM_{10} sampling head. Particles
129 were collected on $0.6\ \mu\text{m}$ polycarbonate filters and transferred into centrifuge tubes. The system was cleaned manually and
130 flushed for 10 min with pure nitrogen before loading a new sample. A soil sample from Libya (Soil 5, 32.29237N/22.30437E)
131 was dry sieved to $63\ \mu\text{m}$ and used as an analogue for a Saharan mineral dust precursor to make a comparison between CFA
132 and mineral dust.

133 **2.2 Fe dissolution kinetics**

134 The Fe dissolution kinetics of the CFA samples were determined by time-dependent leaching experiments. We followed a
135 similar methodology as in Ito and Shi (2016). PM_{10} fractions were exposed to H_2SO_4 solutions at pH 1, 2 or 3, in the presence
136 of $\text{H}_2\text{C}_2\text{O}_4$ and/or $(\text{NH}_4)_2\text{SO}_4$ to simulate acidic processing in aerosol conditions. The concentration of $\text{H}_2\text{C}_2\text{O}_4$ in the
137 experiment solutions was chosen based on the molar ratio of oxalate and sulfate in $\text{PM}_{2.5}$ (particles with an aerodynamic
138 diameter smaller than $2.5\ \mu\text{m}$) from observations over the East Asia region (Yu et al., 2005). Around 50 mg of CFA was
139 leached in 50 ml of acidic solution to obtain a particles/liquid ratio of $1\ \text{g}\ \text{L}^{-1}$. The sample solution was mixed continuously on
140 a rotary mixer, in the dark at room temperature. A volume of 0.5 mL was sampled at fixed time intervals (2.5, 15, 60 min and
141 2, 6, 24, 48, 72, and 168 hours after the CFA sample was added to the experiment solution) and filtered through $0.2\ \mu\text{m}$ pore
142 size syringe filters. The dissolved Fe concentration in the filtrate was determined using the ferrozine method (Viollier et al.,
143 2000). Leaching experiments were also conducted on the Libyan dust precursor sample. The relative standard deviation (RSD)
144 at each sampling time varied from 4 % to 15 % ($n=7$).

145 The pH of all the experiment solutions was calculated using the E-AIM model III for aqueous solutions (Wexler and Clegg,
146 2002). In part this was because the high ionic strength generated by the elevated concentration of $(\text{NH}_4)_2\text{SO}_4$ prevents
147 electrochemical sensors from making accurate pH measurements. For the experiment solutions with no $(\text{NH}_4)_2\text{SO}_4$, the pH
148 was measured by a pH meter before adding the ash and at the end of the experiments. The solution pH increased after adding
149 the ash, and the change in pH was used to estimate the buffer capacity of alkaline minerals in the samples, including for

150 example calcium carbonates (CaCO_3), lime (CaO), and portlandite (Ca(OH)_2). The estimated concentration of H^+ buffered was
151 used to input the concentration of H^+ into the E-AIM model. For each experiment, the pH was calculated before adding the
152 CFA samples and at the end of the experiments. The pH of the original solution before adding the samples was estimated from
153 the molar concentrations (mol L^{-1}) of H_2SO_4 , $\text{H}_2\text{C}_2\text{O}_4$ and $(\text{NH}_4)_2\text{SO}_4$ used to prepare the solution. The model inputs included
154 the total concentrations of H^+ (without $\text{H}_2\text{C}_2\text{O}_4$ contribution), NH_4^+ , SO_4^{2-} and $\text{H}_2\text{C}_2\text{O}_4$. For the experiment solutions with no
155 $(\text{NH}_4)_2\text{SO}_4$, we calculated the final pH by reducing the total H^+ concentration input into the model to match the pH measured
156 at the end of the experiments. The buffered H^+ was then estimated from the difference between the original and final H^+
157 concentration input into the model. To determine the final pH of the solutions with high ionic strength, the H^+ concentration
158 input in the model was calculated as the difference between the H^+ concentration in the original solution and the buffered H^+
159 estimated at low ionic strength.

160 For the solution with no $(\text{NH}_4)_2\text{SO}_4$, the difference between calculated and measured pH is $<7\%$. Table S1 reports the
161 concentrations of H_2SO_4 , $\text{H}_2\text{C}_2\text{O}_4$ and $(\text{NH}_4)_2\text{SO}_4$ in the experiment solutions, the original and final pH from model estimates
162 (including H^+ concentrations and activities), and the pH measurements for the solution with low ionic strength.

163 **2.3 Sequential extractions**

164 The content of Fe oxide species in the samples was determined by Fe sequential extraction (Baldo et al., 2020; Poulton and
165 Canfield, 2005; Raiswell et al., 2008; Shi et al., 2011b). The Fe oxide species included highly reactive amorphous Fe oxide-
166 hydroxide (FeA), crystalline Fe oxide-hydroxide, mainly goethite and hematite (FeD), and Fe associated with magnetite (FeM).

167 To extract FeA, samples were leached in an ascorbate solution buffered at pH 7.5 (Raiswell et al., 2008; Shi et al., 2011b). The
168 ascorbate solution contained a deoxygenated solution of 50 g L^{-1} sodium citrate, 50 g L^{-1} sodium bicarbonate, and 10 g L^{-1} of
169 ascorbic acid. Around 30 mg of CFA was leached for 24 hours in 10 mL of ascorbate extractant, mixed continuously on a
170 rotary mixer. The extraction solution was then filtered through a $0.2 \mu\text{m}$ membrane filter. In order to extract FeD, the residue
171 was leached for 2 more hours in a dithionite solution buffered at pH 4.8 (50 g L^{-1} sodium dithionite in 0.35 M acetic acid and
172 0.2 M sodium citrate) (Raiswell et al., 2008; Shi et al., 2011b).

173 For the extraction of FeM, the CFA samples were first leached for 2 hours using a citrate-buffered dithionite solution to remove
174 FeD. The residue collected after filtration was then leached for 6 hours in a solution of 0.2 M ammonium oxalate ($(\text{NH}_4)_2\text{C}_2\text{O}_4$)
175 and 0.17 M $\text{H}_2\text{C}_2\text{O}_4$ at pH 3.2 (Poulton and Canfield, 2005). The Fe extractions were all carried out in the dark at room
176 temperature. The Fe concentration in the filtered extraction solutions was measured using the ferrozine method (Viollier et al.,
177 2000) or by inductively coupled plasma optical emission spectrometry (ICP-OES) analysis for the solutions containing high
178 concentration of oxalate.

179 The total Fe content in the samples was determined by microwave digestion in concentrated nitric acid (HNO_3) followed by
180 inductively coupled plasma mass spectrometry (ICP-MS) analysis. A detailed description of the digestion method is provided
181 in the supporting information (Text S1). The total Fe content obtained for the Arizona Test Dust (ATD, Iso 12103-1, Power
182 Technology, Inc.) was comparable with the latest consensus value for the total Fe in ATD which indicates a good recovery
183 ($94.0\% \pm 1.5\%$). The recovery of Fe assessed using a standard reference material for urban particulate matter (NIST SRM
184 1648A) was $89.0\% \pm 0.4\%$. It is possible that some of the Fe in aluminosilicate minerals are not fully digested but the
185 uncertainty associated with this analytical method is very small, particularly when we compare this with the large uncertainty
186 in simulated Fe solubility in models.

187 The sequential extraction techniques were tested using the ATD. The wt% of Fe obtained for each extract using the ATD was
188 0.057 ± 0.002 for FeA, 0.394 ± 0.045 for FeD, 0.047 ± 0.006 for FeM (n=7) and 3.501 ± 0.056 for the total Fe (n=3). A
189 summary of the results for the ATD is reported in Table S2.

190 **2.4 X-ray absorption near edge structure (XANES) analysis**

191 We collected XANES spectra to qualitatively examine the Fe speciation in the CFA samples. The XANES spectra at the Fe
192 K-edge were collected at the Diamond Light Source beamline I18. A Si(111) double-crystal monochromator was used in the
193 experiments. The beam size was $400 \mu\text{m} \times 400 \mu\text{m}$. The XANES spectra were collected from 7000 to 7300 eV at a resolution
194 varying from 0.2 eV for 3 s in proximity to the Fe K-edge (7100–7125 eV) to 5 eV for 1 s from 7100 to 7300 eV. Powder
195 samples were suspended in methanol and deposited on Kapton[®] tape. The analysis was repeated three times. We measured the
196 XANES spectra of the CFA-PM₁₀ fractions and mineral standards including hematite, magnetite, and illite. Data were
197 processed using the Athena program, part of the software package Demeter (version 0.9.26) (Ravel and Newville, 2005).

198 **2.5 Model description**

199 This study used the Integrated Massively Parallel Atmospheric Chemical Transport (IMPACT) model (Ito et al., 2021a and
200 references therein). The model simulates the emission, chemistry, transport, and deposition of Fe-containing aerosols and the
201 precursor gases of inorganic and organic acids. The coating of acidic species on the surface of Fe-containing aerosols promotes
202 the release of soluble Fe in the aerosol deliquescent layer and enhances the aerosol Fe solubility (Li et al., 2017). On the other
203 hand, the external mixing of oxalate-rich aerosols with Fe-rich aerosols can suppress the oxalate-promoted Fe dissolution at
204 low concentration of oxalate near the source regions (Ito, 2015). However, the internal mixing of alkaline minerals such as
205 calcium carbonate with Fe-containing dust aerosols can suppress the Fe dissolution (Ito and Feng, 2010). Since CFA particles
206 are co-emitted with acidic species, the transformation of relatively insoluble Fe in coal combustion aerosols into dissolved Fe
207 is generally much faster than that for mineral dust aerosols during their atmospheric lifetime (Ito, 2015; Ito and Shi, 2016).
208 Additionally, the size of CFA particles is substantially smaller than that of mineral dust. Thus, we adopted an observationally
209 constrained parameter for the dry deposition scheme (Emerson et al., 2020) to improve the simulation of dry deposition velocity
210 of fine particles.

211 To improve the accuracy of our simulations of Fe-containing aerosols, we revised the on-line Fe dissolution schemes in the
212 original model (Ito et al., 2021a) in conjunction with a more dynamic range of pH estimates. To apply the Fe dissolution
213 schemes for high ionic strength in aerosols, we used the mean activity coefficient for pH estimate (Pye et al., 2020). Moreover,
214 the dissolution rate was assumed to be dependent of pH for highly acidic solutions (pH < 2) unlike in the former dissolution
215 scheme (Ito, 2015), which allowed us to predict the sensitivity of Fe dissolution to pH lower than 2.

216 To validate the new dissolution scheme, we compared our model results with observations of Fe solubility in PM_{2.5} aerosol
217 particles over the Bay of Bengal (Bikkina et al., 2020).

218 **3 Experimental results**

219 **3.1 Fe dissolution kinetics**

220 We determined that Krakow ash had the largest buffer capacity, around 0.008 moles of buffered H⁺ per litre, which was related
221 to the content of alkaline minerals in the sample. The buffer capacity of Aberthaw and Shandong ash was ~10 times smaller
222 than that of Krakow ash, around 0.0007 moles of buffered H⁺ per litre. Leaching Krakow ash in 0.005 M H₂SO₄, the initial
223 concentration of H⁺ was similar to the concentration of the H⁺ buffered. As a result, the solution pH raised from

224 approximately 2.1 to 2.7 corresponding to a pH change of around 20% (Table S1). For all the other experimental conditions,
225 the pH change was below 12% (Table S1). At the pH conditions used in this study (pH 1-3), acid buffering was fast and likely
226 occurred within the first 1-2 hours. We assumed that the calculated final pH was representative of the solution pH over the
227 duration of the experiments. The leaching experiments were conducted up to 168 h to better capture the dissolution curve in
228 the kinetic model but also considering the tropospheric lifetime of aerosol particles.

229 Dissolved Fe at different time intervals is reported as Fe%, which is the fraction of Fe dissolved to the total Fe content (FeT)
230 in the CFA samples. For all samples, a fast dissolution rate was observed at the beginning of the experiment. In the case of
231 Krakow ash, the dissolution plateau was reached after 2-hour leaching in 0.005 M H₂SO₄ as sufficient Fe may be dissolved
232 from the highly reactive Fe species to suppress the dissolution of less reactive Fe. For that sample/initial condition the pH
233 increased to 2.7, and no more Fe was dissolved, leading to a total Fe solubility of ~9% over the duration of the experiment (7
234 days) (Fig. 1a). Dissolving Krakow ash in 0.01 M H₂SO₄ (Fig. 1a), the experiment solution had a final calculated pH of 2.1.
235 The total Fe solubility was 34% at pH 2.1, almost 4 times higher than that at pH 2.7 (in 0.005 M H₂SO₄). Dissolution of
236 Aberthaw and Shandong ash was slower compared to Krakow ash (Figs. 1b and 2c, respectively). Leaching Aberthaw and
237 Shandong ash in 0.005 M H₂SO₄ resulted in solutions with a pH of around 2.2. At this pH, the total Fe solubility was 18% for
238 Aberthaw ash and 21% for Shandong ash, which is 9-10 times higher than the total Fe solubility at pH 2.9 (in 0.001 M H₂SO₄),
239 around 2% for both samples.

240 The experimental treatment of dissolved Fe from Krakow ash in 0.05 M H₂SO₄ solution with 1 M (NH₄)₂SO₄ (Fig. 1a) resulted
241 in a final predicted pH of 2.1. At that pH, the total Fe solubility of Krakow ash increased from 34% with no (NH₄)₂SO₄ to 48%
242 with high (NH₄)₂SO₄ concentration. The total Fe solubility of Krakow ash was around 28% at pH 3.0 with 1 M (NH₄)₂SO₄
243 (Fig. 1a), 3 times higher than that at pH 2.7 with no (NH₄)₂SO₄. At around pH 2, the total Fe solubility of Aberthaw (Fig. 1b)
244 and Shandong ash (Fig. 1c) increased by around 20% and 30% in the presence of (NH₄)₂SO₄. By contrast, the total Fe solubility
245 at pH 3.1 with 1 M (NH₄)₂SO₄ was 7.5% for Aberthaw ash (Fig. 1b) and 14% for Shandong ash (Fig. 1c), respectively, which
246 was around 4 and 7 times higher than in the experiments carried out at pH 2.9 without (NH₄)₂SO₄.

247 The Fe dissolution of the CFA samples in H₂SO₄ solutions with 0.01 M H₂C₂O₄ (at around pH 2) is shown in Fig. 2. The total
248 Fe solubility of Krakow ash at pH 1.9 with 0.01 M H₂C₂O₄ was 61% (Fig. 2a), which was almost 2 times higher than that at
249 pH 2.1 but without H₂C₂O₄ (Fig. 2a). For Aberthaw ash, oxalate contribution to the dissolution process led to a total Fe
250 solubility of 30% at pH 2.0 (Fig. 2b), which was 70% higher than in the experiment carried out in 0.005 M H₂SO₄ (~pH 2.2)
251 (Fig. 2b). Shandong ash dissolution behaviour was not affected by the presence of oxalate (Fig. 2c).

252 We also investigated the effect of high (NH₄)₂SO₄ concentration on oxalate-promoted dissolution. In Fig. 2a, the total Fe
253 solubility of Krakow ash decreased from 61% at pH 1.9 in the presence of oxalate to 54% at pH 2.0 with oxalate and (NH₄)₂SO₄.
254 For Aberthaw ash, the total Fe solubility at pH 2.0 decreased from 30% in the presence of oxalate to 19% after the addition of
255 (NH₄)₂SO₄ (Fig. 2b).

256 Figure 3 shows the Fe dissolution behaviour of Krakow ash at different pH conditions in the presence of 1 M (NH₄)₂SO₄ and
257 H₂C₂O₄ (0.01-0.03 M depending on the solution pH). The total concentration of oxalate ions was calculated using the E-AIM
258 model and was similar at different pH conditions, 0.015 at pH 1.0 (Experiment 7 Table S3), 0.009 at pH 2.0, and 0.01 at pH
259 2.9 (Experiments 3 Table S3). The highest total Fe solubility was observed at pH 1.0 (~67%). At pH 2.0, the total Fe solubility
260 decreased to 54%, and no substantial variations were observed between pH 2.0 and pH 2.9 (54%-51%). At pH 1.0, the
261 concentration of H⁺ was considerably higher compared to pH 2.0-2.9, leading to a faster dissolution rate. The total
262 concentration of oxalate ions was 1.5-1.6 times higher in the solution at pH 1.0 than at pH 2.0-2.9, which may also contribute
263 to the faster dissolution rate. C₂O₄²⁻ concentration increased with rising pH. Although the concentration of H⁺ was lower at pH

264 2.9 than at pH 2.0, the E-AIM model estimated that $C_2O_4^{2-}$ contributed around 35% of the total oxalate concentration at pH
265 2.9, which was 4.5 times higher than at pH 2.0 (Experiments 3 Table S3). The similar dissolution behaviour at pH 2.0 and pH
266 2.9 conditions may reflect the combination of these two opposite factors, higher concentration of $C_2O_4^{2-}$ but lower
267 concentration of H^+ at pH 2.9 compared to 2.0.

268 We determined the Fe dissolution behaviour of Krakow ash at pH 1.0 in the presence of oxalate and increasing concentrations
269 of $(NH_4)_2SO_4$. The ash was leached in H_2SO_4 solutions with 0.03 M $H_2C_2O_4$ at pH 1.0, while the concentration of $(NH_4)_2SO_4$
270 varied from 0 to 1.5 M. In Fig. 4, the total Fe solubility of Krakow ash in the presence of oxalate was 75% at pH 1.0 and
271 decreased to 68% after the addition of 0.5 M $(NH_4)_2SO_4$. Higher $(NH_4)_2SO_4$ concentrations did not affect the Fe dissolution
272 behaviour in the presence of oxalate at pH 1.0.

273 3.2 Fe speciation

274 The Fe-bearing phases in the CFA samples determined through sequential extractions are shown in Fig. 5c. The Fe speciation
275 in the Libyan dust precursor is added for comparison. Krakow ash had a total Fe (FeT) content of 5.2%, while FeT in Aberthaw
276 and Shandong ash was 3.1% and 1.6% respectively. Amorphous Fe (FeA/FeT) was 6.5% in Krakow ash, 2% in Aberthaw ash,
277 and 4.6% in Shandong ash. The CFA samples showed very different dithionite Fe (FeD/FeT) content, 21.5% in Krakow ash,
278 8% in Aberthaw ash and 14.8% in Shandong ash. The content of magnetite (FeM/FeT) was considerably higher in Krakow
279 ash (22.4%) compared to Aberthaw (2.9%) and Shandong (4.5%) ash. About 50%–87% of Fe was contained in other phases
280 most likely in aluminosilicates. Overall, CFA had more magnetite and highly reactive amorphous Fe and less dithionite Fe
281 than the Libyan dust precursor sample.

282 In Figs. 5a-b, the Fe K-edge XANES spectra of Krakow and Aberthaw ash showed a single peak in the pre-edge region at
283 around 7114.3 eV and 7114.6 eV, respectively. In the edge region, Aberthaw ash showed a broad peak at around 7132.2 eV,
284 while the peak of Krakow ash was slightly shifted to 7132.9 eV and narrower. The pre-edge peak at around 7115.4 suggests
285 that Fe was mainly as Fe(III). The spectral features of Aberthaw and Krakow ash are different from those of the hematite,
286 magnetite and illite standards suggesting that the glass fraction was dominant and controlled their spectral characteristics,
287 which is consistent with the results of the Fe sequential extractions. The XANES Fe K-edge spectra of the CFA samples have
288 some common features with those of Icelandic dust but tend to differ from mineral dust sourced in the Saharan dust source
289 region. In the pre-edge region of the spectrum, Icelandic dust (sample D3 in Figs. 5a-b) showed a main peak at around
290 7114.4 eV and a second less intense peak at around 7112.7 eV, while a broad peak was observed at around 7131.9 eV in the
291 edge region (Baldo et al., 2020). A mineral dust sample from the western Sahara (WS dust in Figs. 5a-b) showed a distinct
292 double peak in the pre-edge region at around 7113.9 and 7115.2 eV, and a main peak in the edge region at around 7133.3 eV
293 (Baldo et al., 2020). The similarities between Icelandic ash and CFA could be because aluminium silicate glass is dominant in
294 these samples (e.g., Baldo et al., 2020; Brown et al., 2011), while Fe-bearing phases in mineral dust from the Saharan region
295 are primarily iron oxides minerals such as hematite and goethite, clay minerals and feldspars (e.g., Shi et al., 2011b).

296 4 Fe simulation from the IMPACT model

297 4.1 Fe dissolution scheme

298 Based on the laboratory experiments carried out on the CFA samples, we implemented a 3-step dissolution scheme for proton-
299 promoted and oxalate-promoted Fe dissolution (Table 1). The Fe dissolution kinetics were described as follows (Ito, 2015):

$$300 \sum_i RFe_i = k_i(pH, T) \times a(H^+)^{m_i} \times f_i \quad (1)$$

301 where RFe_i is the dissolution rate of individual mineral i , k_i is the rate constant (moles Fe $g^{-1} s^{-1}$), $a(H^+)$ is the H^+ activity in
 302 solution, m_i represents the empirical reaction order for protons. The function f_i ($0 \leq f_i \leq 1$) accounts for the suppression of
 303 mineral dissolution by competition for oxalate between surface Fe and dissolved Fe (Ito, 2015):

$$304 \quad f_i = 0.17 \times \ln([\text{lig}] \times [Fe]^{-1})_i + 0.63 \quad (2)$$

305 in which, $[Fe]$ is the molar concentration (mol L^{-1}) of Fe^{3+} dissolved in solution, and $[\text{lig}]$ is the molar concentration of ligand
 306 (e.g., oxalate). f_i was set to 1 for the proton-promoted dissolution.

307 The scheme assumes 3 rate constants “fast”, “intermediate” and “slow” for the proton-promoted, and the proton + oxalate-
 308 promoted dissolution (Table 1). These were obtained by fitting the parameters to our measurements for Krakow ash in H_2SO_4
 309 and $(NH_4)_2SO_4$ at pH 2-3, with and without oxalate (Experiments 2 and 3 in Table S1), which are shown in Fig. 6. The fast
 310 rate constant represents highly reactive Fe species such as amorphous Fe oxyhydroxides, Fe carbonates and Fe sulfates. The
 311 intermediate rate constant can be applied to nano-particulate Fe oxides, while more stable phases including for example Fe-
 312 aluminosilicate and crystalline Fe oxides have generally slower rates (Ito and Shi, 2016; Shi et al., 2011a; Shi et al., 2011b;
 313 Shi et al., 2015). Similarly, we predicted the dissolution kinetics of Aberthaw ash and Shandong ash (Fig. 7). The dissolution
 314 kinetics of Krakow ash were calculated based also on the experimental results at pH 1.0, which is shown in Fig. S2 in
 315 comparison with kinetics predicted at pH 2.0 and pH 2.9 conditions.

316 The contribution of the oxalate-promoted dissolution to dissolved Fe was derived as the difference between the estimated
 317 dissolution rates for the proton + oxalate-promoted dissolution and the proton-promoted dissolution:

$$318 \quad RFe_{i(\text{oxalate})} = RFe_{i(\text{proton} + \text{oxalate})} - RFe_{i(\text{proton})} \quad (3)$$

319 The Fe dissolution rates were predicted at a wider range of pH using Eq. (1) and Eq. (3) and the parameters in Table 1:

$$320 \quad RFe_i = RFe_{i(\text{proton} + \text{oxalate})} \text{ when } RFe_{i(\text{oxalate})} < 0 \quad (4)$$

321 Since $RFe_{i(\text{oxalate})}$ is less than 0 at low pH (< 2), this equation applies to highly acidic conditions. As a result, the predicted
 322 amount of dissolved Fe was smaller when using the dissolution rate for the proton + oxalate-promoted dissolution, $RFe_{i(\text{proton} +$
 323 $\text{oxalate})}$, rather than the rate for the proton-promoted dissolution, $RFe_{i(\text{proton})}$, at pH < 2 . Accordingly, the dissolution rate, RFe_i ,
 324 was less dependent on the pH compared to $RFe_{i(\text{proton})}$ at highly acidic conditions, possibly due to the competition for the
 325 formation of surface complexes.

326 At pH > 2 when oxalate does promote Fe dissolution, the following equation applies:

$$327 \quad RFe_i = RFe_{i(\text{proton})} + RFe_{i(\text{oxalate})} \text{ when } RFe_{i(\text{oxalate})} > 0 \quad (5)$$

328 **4.2 Aerosol Fe solubility over the Bay of Bengal**

329 The new dissolution scheme was applied in the IMPACT atmospheric chemistry transport model to predict the Fe solubility
 330 in atmospheric particles collected over the Bay of Bengal, which is an area for which there are detailed field measurements
 331 available (Bikkina et al., 2020; Kumar et al., 2010; Srinivas and Sarin, 2013; Srinivas et al., 2012) and multi-modelling analyses
 332 have been done (Ito et al., 2019). It thus represents a test for our experimental results in actual field conditions. Three sensitivity
 333 simulations were performed to explore the effects of the uncertainties associated with the dissolution schemes and
 334 mineralogical component of Fe. In addition, the former setting (Ito et al., 2021a) was used in the IMPACT model for
 335 comparison.

336 For all simulations, the total Fe emissions from anthropogenic combustion sources and biomass burning were estimated using
337 the Fe emission inventory of Ito et al. (2018) including also emissions from the iron and steel industry, whereas Fe emissions
338 from mineral dust sources were dynamically simulated (Ito et al., 2021a). In Test 0, we ran the model without the upgrades of
339 the dissolution scheme discussed in section 2.4, and apply in addition the photo-induced dissolution scheme for both
340 combustion and dust aerosols (Ito, 2015; Ito and Shi, 2016), which was turned off in Test 1, Test 2, and Test 3 due to the lack
341 of laboratory measurements under high ionic strength. To estimate the aerosol pH, we applied a H^+ activity coefficient of 1 for
342 Test 0, while the mean activity coefficient from Pye et al. (2020) was used for the other tests. The dissolution rate was assumed
343 as pH-independent for highly acidic solutions ($pH < 2$) (Ito, 2015) in Test 0, based on the laboratory measurements in Chen et
344 al. (2012), while no pH threshold was considered in Test 1, Test 2, and Test 3 as the total dissolution (proton + oxalate) was
345 suppressed at $pH < 2$ from the predicted dissolution rate.

346 In Test 1, we used the new dissolution scheme accounting for the proton- and oxalate- promoted dissolution of Krakow ash
347 for all combustion aerosols in the model (Table 1). The dissolution kinetics were calculated using the base mineralogy for
348 anthropogenic Fe emissions reported in Table S11 of Rathod et al. (2020). The Fe composition of wood was used for open
349 biomass burning (Matsuo et al., 1992). In this simulation, three Fe pools were considered. Sulfate Fe in Rathod et al. (2020)
350 was assumed as fast pool, magnetite Fe as intermediate pool, hematite, goethite and clay as slow pool. In Test 2, we calculated
351 the dissolution kinetics only considering the proton-promoted dissolution. In Test 3, the Fe pools were as determined here for
352 Krakow ash: ascorbate Fe (FeA) as fast pool, magnetite Fe (FeM) as intermediate pool, hematite plus goethite Fe (FeD) and
353 other Fe as slow pool (Fig. 5). FeA contains highly reactive Fe species with fast dissolution rates (Raiswell et al., 2008; Shi et
354 al., 2011b). FeM appeared to work well for the different fly ash samples in the dissolution scheme as intermediate Fe pool.
355 FeD is associated with crystalline Fe oxides which are mostly highly insoluble (Raiswell et al., 2008; Shi et al., 2011b), thus
356 it was considered as slow pool in the dissolution scheme. We assumed other Fe to be mostly Fe-bearing aluminosilicates and
357 considered this as slow Fe pool.

358 Observations of total Fe concentration and Fe solubility in $PM_{2.5}$ along the cruise tracks over the Bay of Bengal for the period
359 extending from 27 December 2008 to 26 January 2009 (Bikkina et al., 2020) were compared with temporally and regionally
360 averaged data from model estimates. The daily averages of model results were calculated from hourly mass concentrations in
361 the air over the surface ocean along the cruise tracks. The concentration of total Fe observed over the Bay of Bengal varies
362 from $145 \pm 144 \text{ ng m}^{-3}$ over the North Bay of Bengal (27 December 2008 - 10 January 2009) to $55 \pm 23 \text{ ng m}^{-3}$ over the South
363 Bay of Bengal (11-26 January 2009) (Bikkina et al., 2020). In Fig. 8, the modelled concentrations of total Fe exhibit a similar
364 variability to that of measurements with relatively higher values over the North Bay of Bengal ($59 \pm 29 \text{ ng m}^{-3}$ in different
365 sensitivity simulations) compared to the South Bay of Bengal ($20 \pm 12 \text{ ng m}^{-3}$ in different sensitivity simulations). However,
366 the modelled concentrations of total Fe were underestimated by a factor of 2.9 ± 1.5 . The model reproduced the source
367 apportionment of Fe (Fig. 8 - Table S4) which is qualitatively derived from previous observational studies indicating that the
368 concentrations of total Fe in aerosols over the North Bay of Bengal are influenced by emissions of dust and combustion sources
369 from the Indo-Gangetic Plain (Kumar et al., 2010), whereas combustion sources (e.g., biomass burning and fossil-fuel) from
370 South-East Asia are dominant over the South Bay of Bengal (Kumar et al., 2010; Srinivas and Sarin, 2013). On the other hand,
371 the model could not reproduce the peak in total Fe concentration (1.8% of Fe content in $PM_{2.5}$ sample) reported around 29
372 December 2008. The total Fe observed in PM_{10} (430 ng m^{-3}) on 29 December 2008 is lower than that measured on the day
373 before (667 ng m^{-3}) and the day after (773 ng m^{-3}), whereas that in $PM_{2.5}$ peaked on 29 December 2008 (Srinivas et al., 2012).
374 Thus, the extreme value recorded only for $PM_{2.5}$ on this date may be an outlier. But we do not have sufficient data to confirm
375 this. One of the possibilities is that the sample collected aerosol particles from a mixture of different aerosols sources (e.g.,
376 dust and anthropogenic aerosols). This reflects one of the challenges of modelling such a dynamic parameter.

377 The comparison of Fe solubility using the same total Fe emissions directly represents the effect of the new dissolution scheme
378 on PM_{2.5}. The aerosol Fe solubility measured over the South Bay of Bengal is higher than that over the North Bay of Bengal,
379 respectively 32% ± 11% and 15% ± 7% (Bikkina et al., 2020), and model estimates showed a similar trend (Fig. 9). In Fig. 9
380 and Table S5, the calculated Fe solubilities over the North Bay of Bengal in Test 1 (11% ± 4%), Test 2 (17% ± 5%), and Test
381 3 (17% ± 6%) were in good agreement with observations. The aerosol Fe solubility over the South Bay of Bengal was better
382 captured in Test 1 (30% ± 5%) and Test 3 (37% ± 7%), whereas Test 0 showed higher variability (37% ± 22%). The proton-
383 promoted dissolution scheme in Test 2 significantly overestimated the Fe solubility over the Bay of Bengal (Fig. 9 and Table
384 S5). The aerosol Fe solubility was largely overestimated in all scenarios after 22 January 2009, as open biomass burning
385 sources become dominant (Fig. 8 and Table S4).

386 The comparison between observations and model predictions of aerosol Fe solubility over the Bay of Bengal is shown in Fig.
387 S3. The agreement between measurements and model predictions was the best in Test 1 and Test 3. These exhibited good
388 correlation with observations ($R = 0.49$ in Test 1 and $R = 0.54$ in Test 3), and the lowest root mean squared difference between
389 the simulated and observed Fe solubilities (RMSE = 11 in Test 1 and RMSE = 12 in Test 3). In Test 0, the model estimates
390 showed a greater difference from observations (RMSE = 21) and poor correlation ($R = 0.26$).

391 **5 Discussion**

392 **5.1 Dissolution behaviour of Fe in CFA**

393 In this study, the Fe dissolution kinetics of CFA samples from UK, Poland and China were investigated under simulated
394 atmospheric acidic conditions. A key parameter in both the atmosphere and the simulation experiments is the pH of the water
395 interacting with the CFA particles. The lower the pH of the experimental solution the faster the dissolution and eventually the
396 higher the amount of Fe dissolved. Our results showed a strong pH dependence in low ionic strength conditions, with higher
397 dissolution rates at lower pH. For example, reducing the solution pH from 2.7 to 2.1, the Fe solubility of Krakow ash in H₂SO₄
398 only increased by a factor of 4 (Fig. 1a) over the duration of the experiments, while the Fe solubility of Aberthaw and Shandong
399 ash increased by 9-10 times from pH 2.9 to pH 2.2 (Figs. 1b-c). This enhancement is higher than that observed in studies
400 conducted on mineral dust samples, which showed that one pH unit can lead to 3-4 times difference in dissolution rates (Ito
401 and Shi, 2016; Shi et al., 2011a). Furthermore, Chen et al. (2012) reported that the Fe solubility of the certified CFA 2689 only
402 increased by 10% from pH 2 to pH 1, after 50 hours of dissolution in acidic media. The Fe solubility of CFA (PM₁₀ fractions)
403 after 6 hours at pH 2 was 6%-10% for Aberthaw and Shandong ash respectively, and 28% for Krakow ash (Fig. 1). The Fe in
404 our CFA samples initially dissolved faster than those used by Fu et al. (2012), who reported 2.9%-4.2% Fe solubility in bulk
405 CFA from three coal-fired power plants in China after 12-hour leaching at pH 2. These results suggest that there are
406 considerable variabilities in the pH dependent dissolution of Fe in CFA. This could be due to differences in the Fe speciation
407 between CFA samples and/or the different leaching media used.

408 Our results showed that high ionic strength has a major impact on dissolution rates of CFA at low pH (i.e., pH 2-3). The Fe
409 solubility of CFA increased by approximately 20%-40% in the presence of 1 M (NH₄)₂SO₄ at around pH 2 over the duration
410 of the experiments, and by a factor from 3 to 7 at around pH 3 conditions (Fig. 1). At high ionic strength, the activity of ions
411 in solution is reduced, thus, in order to maintain similar pH conditions, the H⁺ concentration has to be increased (Table S1).
412 Although Fe dissolution was primarily controlled by the concentration of H⁺, the high concentration of sulfate ions could also
413 be an important factor contributing to Fe dissolution, in particular when the concentration of H⁺ in the system was low (e.g.,
414 pH 3). Previous research found that the high ability of anions to form soluble complexes with metals can enhance Fe dissolution
415 (Cornell et al., 1976; Cornell and Schwertmann, 2003; Furrer and Stumm, 1986; Hamer et al., 2003; Rubasinghege et al., 2010;
416 Sidhu et al., 1981; Surana and Warren, 1969). Sulfate ions adsorbed on the particles surface form complexes with Fe (e.g.,

417 Rubasinghege et al., 2010). This may increase the surface negative charge favouring the absorption of H^+ and thereby increase
418 Fe dissolution at the particle surface. In addition, the formation of surface complexes may weaken the bonds between Fe and
419 the neighbouring ions (Cornell et al., 1976; Furrer and Stumm, 1986; Sidhu et al., 1981). Cwiertny et al. (2008) reported that
420 at pH 1-2 the high ionic strength generated by NaCl up to 1 M did not influence Fe dissolution of mineral dust particles.
421 However, Ito and Shi (2016) showed that the high ionic strength resulting from the addition of 1 M $(NH_4)_2SO_4$ in leaching
422 solutions at pH 2-3 enhanced the Fe dissolution of dust particles, which was also observed here for the CFA samples. Borgatta
423 et al. (2016) compared the Fe solubility of CFA from USA Midwest, North-East India, and Europe in acidic solution (pH 1-2)
424 containing 1 M NaCl. The Fe solubility measured after 24 hours varied from 15% to 70% in different CFA (bulk samples) at
425 pH 2 with 1 M NaCl, which was considerably higher than that observed at pH 2 with 1 M $NaNO_3$ (<20%) (Kim et al., 2020).
426 Both studies did not investigate the impact of ionic strength on the dissolution behaviour, i.e., by comparing the dissolution at
427 low and high ionic strength. Note that both studies did not specify how the pH conditions were maintained at pH 2. Here, we
428 considered the most important sources of high ionic strength in aerosol water and simulated Fe dissolution in the presence of
429 $(NH_4)_2SO_4$ and $H_2C_2O_4$ under acidic conditions. We emphasize that the pH under high ionic strength here is estimated from a
430 thermodynamic model, similar to those implemented in the IMPACT model.

431 The presence of oxalate enhanced Fe dissolution in Krakow and Aberthaw ash but not in Shandong ash at around pH 2 (Fig.
432 2). The effect of oxalate on the Fe dissolution kinetics has also been studied by Chen and Grassian (2013) at pH 2 (11.6 mM
433 $H_2C_2O_4$). After 45-hour leaching, the Fe solubility of the certified CFA 2689 increased from 16% in H_2SO_4 at pH 2 to 44% in
434 $H_2C_2O_4$ at the same pH (Chen and Grassian, 2013). Therefore, the enhancement in Fe solubility of CFA in the presence of
435 oxalate observed in this study (from no impact in Shandong ash to doubled dissolution in Krakow ash) is lower than the 2.8
436 time increase in Fe solubility reported for the certified CFA 2689 (Chen and Grassian, 2013). Since no data are available in
437 Chen and Grassian (2013), we are unable to make a comparison with the other two certified CFA samples. The Fe solubility
438 of Krakow ash after 48-hour leaching at pH 1.9 with 0.01 M $H_2C_2O_4$ (Fig. 2a) was 53%, which is within the range of Fe
439 solubilities observed in Chen and Grassian (2013) for the certified CFA samples at similar pH and $H_2C_2O_4$ concentrations
440 (from 44% to 78%), whereas the Fe solubility of Aberthaw and Shandong ash (Figs. 2b-c, 18%-17% after 48-hour leaching at
441 pH 2.0 with 0.01 M $H_2C_2O_4$) was considerably lower than that of certified CFA (Chen and Grassian, 2013). These results
442 suggest a large variability in the effects of oxalate on the Fe dissolution rates in different types of CFA.

443 Our results also indicated that high $(NH_4)_2SO_4$ concentrations suppress oxalate-promoted Fe dissolution of CFA (Fig. 2), which
444 was not considered in previous research. At pH 1.9 in the presence of oxalate, the Fe solubility of Krakow ash decreased by
445 around 10% after the addition of $(NH_4)_2SO_4$, while the Fe solubility of Aberthaw ash decreased by 35% (Fig. 2). We used the
446 E-AIM model to estimate the concentration of oxalate ions and their activity (Table S3). The pH influences the speciation of
447 $H_2C_2O_4$ in solution (e.g., Lee et al., 2007). $H_2C_2O_4$ is the main species below pH 2, whereas $HC_2O_4^-$ is dominant between pH
448 2-4. Above pH 4, $C_2O_4^{2-}$ is the principal species. In our experiments, $H_2C_2O_4$ is mainly as $HC_2O_4^-$ at around pH 2 (Experiments
449 3-4 in Table S3). In the presence of $(NH_4)_2SO_4$, the activity coefficient of $HC_2O_4^-$ was reduced by approximately 35-38%
450 (Experiments 3 in Table S3). Increasing the ionic strength lowers the activity of the oxalate ions, but at the same time favours
451 the dissociation of the acid. At around pH 2 conditions, the E-AIM model estimated that the activity of $C_2O_4^{2-}$ was reduced by
452 around one order of magnitude in the presence of $(NH_4)_2SO_4$, while its concentration increased 12-15 times (Experiments 3 in
453 Table S3). The adsorption of anions can reduce oxalate adsorption on the particle surface due to electrostatic repulsion which
454 results in slower release of Fe (Eick et al., 1999). Precipitation of ammonium hydrogen oxalate ($NH_4HC_2O_4$) can also occur in
455 the system, but this is very soluble and easily re-dissolves forming soluble oxalate species (Lee et al., 2007). We speculate that
456 the high concentration of sulfate ions is likely to be responsible for inhibiting the oxalate-promoted dissolution by reducing
457 oxalate adsorption on the particle surface. At pH 1 in the presence of oxalate, increasing the concentration of $(NH_4)_2SO_4$ from
458 0.5 M to 1.5 M did not affect the Fe dissolution behaviour of the CFA samples (Fig. 4). As previously discussed, the adsorption

459 of sulfate ions on the particle surface may inhibit oxalate-promoted dissolution. However, once the saturation coverage is
460 reached, increasing the concentration of anions has no further effect on the dissolution rate (Cornell et al., 1976).

461 Fe speciation is an important factor affecting the Fe dissolution behaviour. CFA particles have very different chemical and
462 physical properties depending for example on the nature of coal burned, combustion conditions, cooling process and particle
463 control devices implemented at the power stations (e.g., Blissett and Rowson, 2012; Yao et al., 2015). This is likely the reason
464 why the Fe speciation observed in the CFA samples analysed in this study from different locations varied considerably (Fig.
465 5). In the CFA samples, the Fe dissolution curves for different pH and ionic strengths generally showed the greatest rate of Fe
466 release within the first 2 hours, followed by a slower dissolution, reaching almost a plateau at the end of the experimental run.
467 This indicates the presence of multiple Fe-bearing phases in CFA particles with a wide range of reactivity. Initially, highly
468 reactive phases were the main contribution to dissolved Fe. As the dissolution continued, more refractory phases became the
469 dominant source of dissolved Fe (Shi et al., 2011a). SEM analysis conducted on CFA samples showed that CFA particles are
470 mostly spherical (e.g., Chen et al., 2012; Dudas and Warren, 1987; Valeev et al., 2018; Warren and Dudas, 1989) with Fe
471 oxide aggregates on the surface (Chen et al., 2012; Valeev et al., 2018). The analysis of the CFA samples processed in aqueous
472 solution at low pH suggests that initially Fe dissolved from the reactive external glass coating (Dudas and Warren, 1987;
473 Warren and Dudas, 1989) and from the Fe oxide aggregates on the particle surface (Chen et al., 2012; Valeev et al., 2018).
474 Subsequently, Fe is likely realised from the structure of the aluminium silicate glass (Chen et al., 2012; Dudas and Warren,
475 1987; Valeev et al., 2018; Warren and Dudas, 1989), and crystalline Fe oxide phases (Warren and Dudas, 1989). Overall,
476 Krakow ash showed the fastest dissolution rates, but the dissolution of highly reactive Fe species as FeA is insufficient to
477 account for the high Fe solubility observed at low pH. Our results showed that once the FeA dissolved, additional Fe was
478 dissolved from more refractory Fe-bearing phases. The modelled dissolution kinetics obtained using FeM as intermediate pool
479 were in good agreements with measurements (Figs. 7-S2). FeM is likely to be primary magnetite but may contain a fraction of
480 the more reactive aluminosilicate glass. Our model results suggest that magnetite in CFA particles may be more soluble than
481 has been shown in Marcotte et al. (2020). It is possible that in real CFA samples the physicochemical properties of minerals
482 including for example crystal size, degree of crystallinity, cationic and anionic substitution in the lattice which influence the
483 Fe dissolution behaviour (e.g., Schwertmann, 1991) are likely to be different from those of the reference minerals analysed in
484 Marcotte et al. (2020). In order to investigate the links between Fe solubility and Fe speciation/mineralogy, more work is
485 needed to determine the Fe mineralogy in CFA samples at emission and after atmospheric processing, in combination with
486 solubility experiments.

487 Finally, the modelled dissolution kinetics obtained using the new dissolution scheme for CFA (Table 1) showed better
488 agreement with laboratory measurements than when using the original scheme (Ito, 2015) (Fig 10). In Figs. 10a-b, we
489 compared the Fe dissolution kinetics of Krakow ash at around pH 2 and 3 with 1 M $(\text{NH}_4)_2\text{SO}_4$ calculated using the proton-
490 promoted dissolution scheme in Table 1 with the dissolution kinetics calculated at similar pH but using the proton-promoted
491 dissolution scheme for combustion aerosols in Ito (2015) (Table S6). The dissolution scheme in Ito (2015) was based on
492 laboratory measurements conducted at low ionic strength (Chen et al., 2012) and assumed a single Fe-bearing phase in
493 combustion aerosol particles, while the new dissolution scheme considered the high ionic strength of aerosol water and
494 assumed three rate constants, for fast, intermediate and slow kinetics of the different Fe-bearing phases present in CFA particles.
495 The Fe dissolution kinetics obtained using the new dissolution scheme showed a better agreement with measurements and was
496 enhanced compared to the model estimates obtained using the original dissolution scheme (Ito, 2015) for low ionic strength
497 conditions (Figs. 10a-b). Figures 10c-d show the Fe dissolution kinetics of Krakow ash at pH 2.0 and 2.9 with 0.01 M $\text{H}_2\text{C}_2\text{O}_4$
498 and 1 M $(\text{NH}_4)_2\text{SO}_4$ calculated using the proton- and oxalate-promoted dissolution scheme in Table 1 and the dissolution
499 kinetics calculated at similar pH and $\text{H}_2\text{C}_2\text{O}_4$ concentration but using the scheme in Ito (2015) (i.e., single phase dissolution,
500 see Table S6). The Fe dissolution kinetics predicted using the new dissolution scheme had a much better agreement with

501 measurements. Figure 10e shows the suppression of the oxalate-promoted dissolution at pH 2.0 and high $(\text{NH}_4)_2\text{SO}_4$
502 concentrations. At pH 2, the proton-promoted dissolution was comparable to the proton + oxalate-promoted dissolution (Fig.
503 10e), with $R_{\text{Fe(oxalate)}}$ close to zero (see Eq. 3). At pH 2.9, the proton + oxalate-promoted dissolution was higher than the proton
504 + oxalate-promoted dissolution (Fig. 10f), with $R_{\text{Fe(oxalate)}} > 0$ (Eq. 5).

505 Moreover, the new 3-step dissolution scheme better captured the initial fast dissolution of CFA (Fig. 10) which was also
506 observed in previous research (Borgatta et al., 2016; Chen et al., 2012; Chen and Grassian, 2013; Fu et al., 2012; Kim et al.,
507 2020) (except for the certified CFA 2689 in Chen et al. (2012) which showed increasing dissolution rates over the duration of
508 the experiment). Furthermore, the new scheme enabled us to account for the different Fe speciation determined in the CFA
509 samples, which could be a key factor contributing to the different Fe dissolution behaviour observed in the present study and
510 in literature (Borgatta et al., 2016; Chen et al., 2012; Chen and Grassian, 2013; Fu et al., 2012; Kim et al., 2020). In Fig. 7, the
511 dissolution kinetics of Aberthaw and Shandong ash calculated using the dissolution rates in Table 1 and the Fe-bearing phases
512 determined in the samples showed a good agreement with measurements.

513 **5.2 Comparison with mineral dust**

514 High ionic strength also impacted the dissolution rates of the Libyan dust precursor sample at low pH (Fig. S4). At around pH
515 2 conditions, the proton-promoted Fe dissolution of Libyan dust was enhanced by ~40% after the addition of $(\text{NH}_4)_2\text{SO}_4$. At
516 around pH 2 and with 0.01 M $\text{H}_2\text{C}_2\text{O}_4$, the Fe solubility of Libyan dust decreased by ~30% in the presence of $(\text{NH}_4)_2\text{SO}_4$.
517 Overall, the Fe solubility of Libyan dust was lower compared to that observed in the CFA samples. After 168 hour-leaching
518 at pH 2.1 with 1 M $(\text{NH}_4)_2\text{SO}_4$, the Fe solubility of Libyan dust was 7.2% (Fig. S4), which was from around 3 to 7 times lower
519 compared to that of the CFA samples (Fig. 1). At around pH 2 conditions in the presence of oxalate and high $(\text{NH}_4)_2\text{SO}_4$
520 concentration, the Fe solubility of Libyan dust rose to ~13.6% (Fig. S4), which is still 4 times lower than that of Krakow ash
521 and around 1.5 lower than Aberthaw and Shandong ash (Fig. 2). The Fe solubilities of the Libyan dust observed in this study
522 are comparable with those of the Tibesti dust (Tibesti Mountains, Libya, 25.583333N/16.516667E) in Ito and Shi (2016) at
523 similar experimental conditions.

524 The enhanced Fe solubility in CFA compared to mineral dust could be primarily related to the different Fe speciation (Fig. 5).
525 CFA contained more highly reactive Fe and magnetite but less hematite and goethite than mineral dust.

526 Although mineral dust is the largest contribution to aerosol Fe while CFA accounts for only a few percent, atmospheric
527 processing of CFA may result in a larger than expected contribution of bio-accessible Fe deposited to the surface ocean. It is
528 thus important to quantify the amount and nature of CFA in atmospheric particles.

529 **5.3 Comparison of modelled Fe solubility with field measurements**

530 The model results obtained using the new dissolution scheme for the proton + oxalate-promoted dissolution (Table 1) in Test
531 1 and Test 3 provided a better estimate of aerosol Fe solubility over the Bay of Bengal than the other tests (Figs. 9 and S3). At
532 the same time, the new model improved the agreement of aerosol Fe solubility from Test 0 ($68\% \pm 5\%$) to Test 1 ($35\% \pm 2\%$)
533 and Test 3 ($47\% \pm 1\%$) with the field data ($25\% \pm 3\%$) but still overestimated it after 22 January 2009, when open biomass
534 burning sources become dominant (Bikkina et al., 2020) as also shown in Fig. 8 and Table S4. This could be due to the
535 unrepresentative Fe speciation used in Test 1 and Test 3 for biomass burning over the Bay of Bengal. To reduce the uncertainty
536 in model predictions, emission inventories could be improved through a comprehensive characterization of Fe species in
537 combustion aerosol particles.

538 The revised model also enabled us to predict sensitivity to a more dynamic range of pH changes, particularly between
539 anthropogenic combustion and biomass burning by the suppression of the oxalate-promoted dissolution at pH lower than 2. In
540 Test 0, the dissolution rate was assumed to be independent from the pH for extremely acidic solutions (pH <2). The results
541 show that the proton-promoted dissolution scheme in Test 2 significantly overestimated aerosol Fe solubility (Figs. 9 and S3),
542 which indicates the suppression of the proton + oxalate-promoted dissolution at pH < 2. In Fig. S5, the model estimates of
543 aerosol Fe solubility over the Bay of Bengal considerably improved in Test 1 (RMSE 11) compared to Test 0 (RMSE 21), but
544 more work is needed to improve size-resolved Fe emission, transport, and deposition. The model results in Test 1 indicate a
545 larger contribution of anthropogenic combustion sources to the atmospheric Fe loading over East Asia (Fig. 11), but a smaller
546 contribution of biomass burning sources downwind from tropical regions (Fig. 12). We demonstrated that the implementation
547 of the new Fe dissolution scheme, including a rapid Fe release at the initial stage and highly acidic conditions, enhanced the
548 model estimates. However, in Test 1, we turned off the photo-reductive dissolution scheme (Ito, 2015), which was based on
549 the laboratory measurements in Chen and Grassian (2013). To determine the photoinduced dissolution kinetics of CFA
550 particles it is necessary to account for the effect of high concentration of (NH₄)₂SO₄ on photo-reductive dissolution rate which
551 should be considered in future research.

552 **Data availability statement**

553 The new dissolution schemes for the proton-promoted and oxalate-promoted dissolution are reported in Table 1. Table S1
554 reports the concentrations of H₂SO₄, H₂C₂O₄ and (NH₄)₂SO₄ in the experiment solutions, the original and final pH from model
555 estimates (including H⁺ concentrations and activities), and the pH measurements for the solution with low ionic strength. Table
556 S3 contains the summary of the concentration and activity of total oxalate ions, C₂O₄²⁻, and HC₂O₄⁻ in the experiment solutions
557 calculated using the E-AIM model III. The observations of the mass concentration of total Fe, dissolved Fe and Fe solubility
558 for the fine mode (PM_{2.5}) over the Bay of Bengal are from Bikkina et al. (2020) and are available at
559 <https://pubs.acs.org/doi/10.1021/acsearthspacechem.0c00063>. The modelled mass concentrations of total Fe in aerosol
560 particles and the aerosol Fe solubilities over the Bay of Bengal are reported in Table S4 and Table S5, respectively. The Fe
561 speciation, the measurements of the Fe dissolution kinetics, and the results of the IMPACT model for each sensitivity
562 simulation (Test 0-3) can be downloaded at: <https://doi.org/10.25500/edata.bham.00000702>.

563 **Author contributions**

564 CB, ZS, and AI designed the experiments and discussed the results. ZS supervised the experimental and data analyses. CB
565 conducted the experiments and the data analysis with contributions from ZS, AI, MDK and ND. ND, ZS and KI performed
566 the XANES measurements. AI developed the model of the dissolution kinetics and performed the model simulations. Krakow
567 and Aberthaw ash were provided by TJ, while Shandong ash was provided by WL. Soil 5 from Libya was collected by ND.
568 CB prepared the article with contributions from MDK and all the other co-authors.

569 **Competing interests**

570 The authors declare that they have no conflict of interest.

571 **Acknowledgments**

572 CB is funded by the Natural Environment Research Council (NERC) CENTA studentship (grant no. NE/L002493/1). Support
573 for this research was provided to AI by JSPS KAKENHI (grant no. 20H04329), Integrated Research Program for Advancing

574 Climate Models (TOUGOU) (grant no. JPMXD0717935715) from the Ministry of Education, Culture, Sports, Science and
575 Technology (MEXT), Japan. We acknowledge Diamond Light Source for time on Beamline/Lab I18 under the Proposals:
576 SP22244-1; SP12760-1; SP10327-1.

577 **Financial support**

578 This research has been supported by the Natural Environment Research Council CENTA-DTP (grant no. NE/L002493/1),
579 JSPS KAKENHI (grant no. 20H04329), the Integrated Research Program for Advancing Climate Models (TOUGOU) (grant
580 no. JPMXD0717935715).

581
582

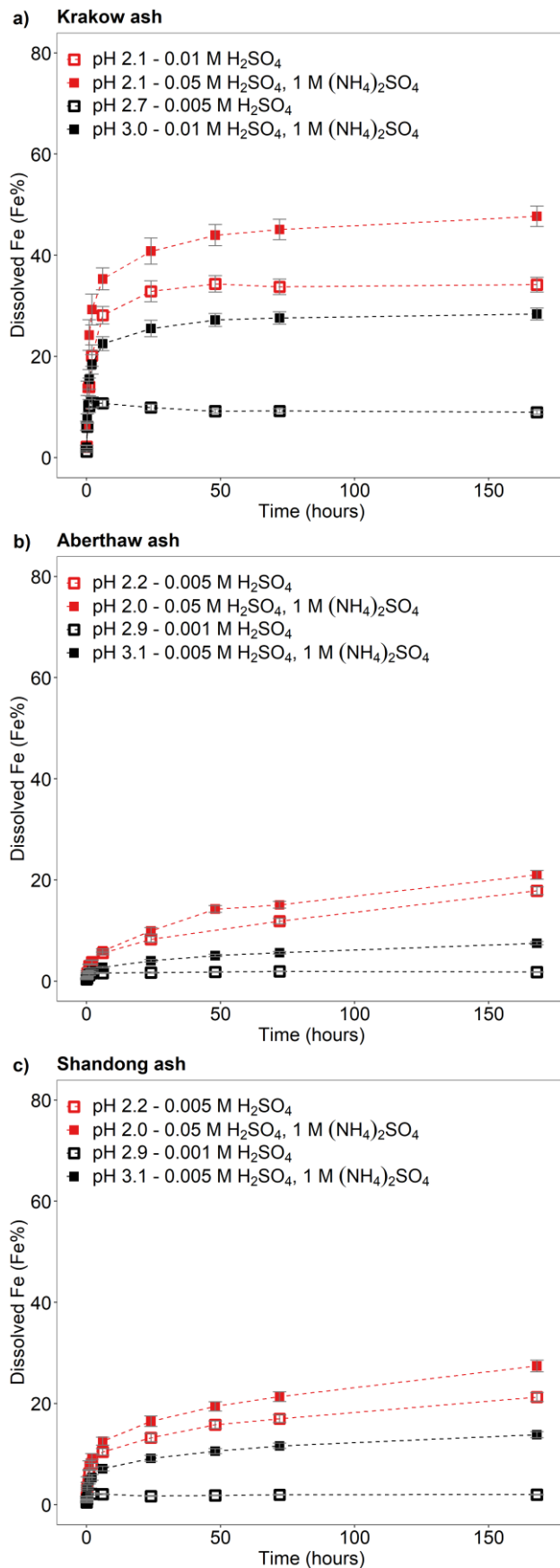
Table 1. Constants used to calculate Fe dissolution rates for fossil fuel combustion aerosols, based on laboratory experiments conducted at high ionic strength.

Stage	Kinetic	Scheme	Rate constant - $k(\text{pH}, T)^a$	m^c
I	Fast	Proton	$7.61 \times 10^{-6} \exp[E(\text{pH})^b \times (1/298 - 1/T)]$	0.241
II	Intermediate	Proton	$1.91 \times 10^{-7} \exp[E(\text{pH})^b \times (1/298 - 1/T)]$	0.195
III	Slow	Proton	$2.48 \times 10^{-7} \exp[E(\text{pH})^b \times (1/298 - 1/T)]$	0.843
I	Fast	Proton + Oxalate	$5.54 \times 10^{-6} \exp[E(\text{pH})^b \times (1/298 - 1/T)]$	0.209
II	Intermediate	Proton + Oxalate	$1.50 \times 10^{-7} \exp[E(\text{pH})^b \times (1/298 - 1/T)]$	0.091
III	Slow	Proton + Oxalate	$1.77 \times 10^{-8} \exp[E(\text{pH})^b \times (1/298 - 1/T)]$	0.204

583 ^a $k(\text{pH}, T)$ is the pH and temperature dependent ‘far-from-equilibrium’ rate constant (moles Fe $\text{g}^{-1} \text{s}^{-1}$). The Fe dissolution
584 scheme assumes 3 rate constants “fast”, “intermediate” and “slow” for the proton- and oxalate-promoted dissolution. The
585 parameters were fitted to our measurements for Krakow ash.

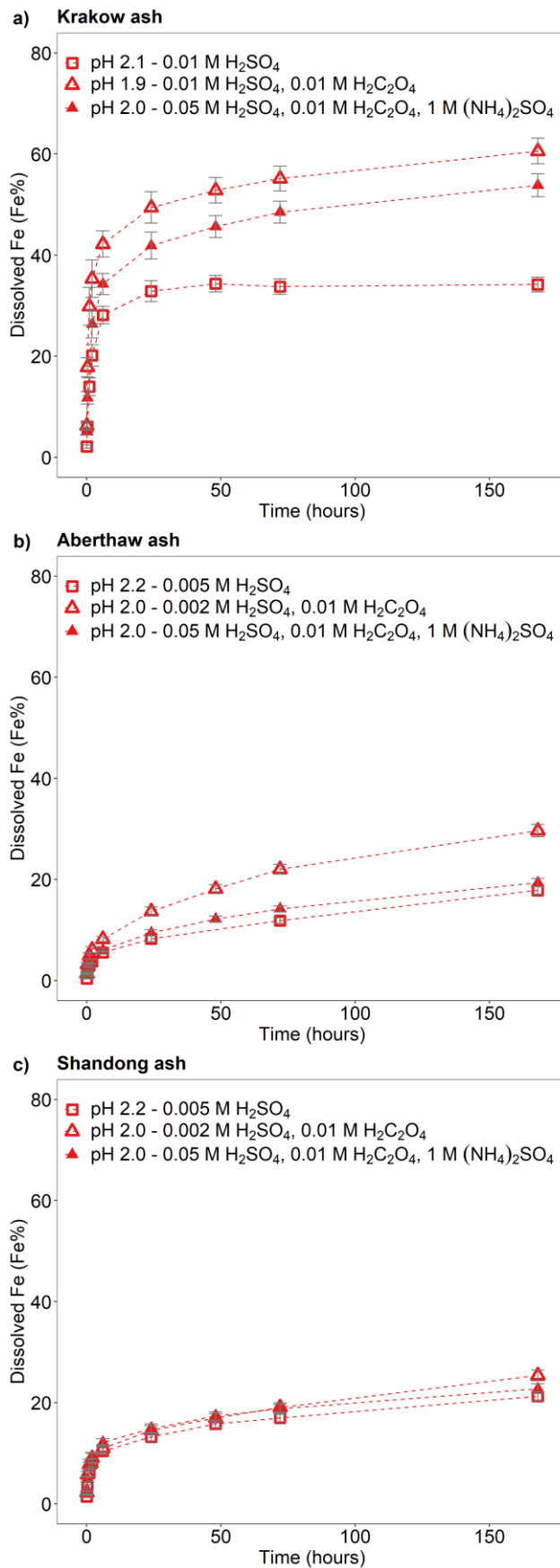
586 ^b $E(\text{pH}) = -1.56 \times 10^3 \times \text{pH} + 1.08 \times 10^4$. The parameters were fitted to the measurements for soils (Bibi et al., 2014).

587 ^c m is the reaction order with respect to aqueous phase protons, which was determined by linear regression from our
588 experimental data in the pH range between 2 and 3 for proton- and oxalate-promoted dissolution schemes.
589



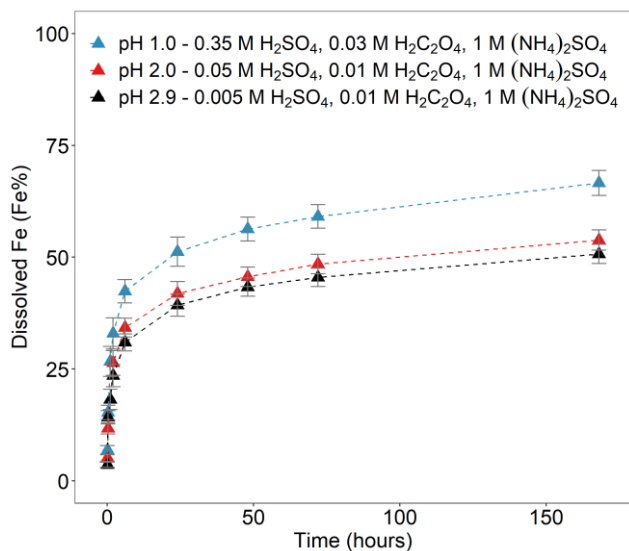
590

591 **Figure 1: Fe dissolution kinetics of a) Krakow ash, b) Aberthaw ash and c) Shandong ash in H₂SO₄ solutions (open rectangles) and**
 592 **with 1 M (NH₄)₂SO₄ (filled rectangles). The molar concentrations of H₂SO₄ and (NH₄)₂SO₄ in the experiment solutions are shown.**
 593 **The final pH of the experiment solutions is also reported, which was calculated using the E-AIM model III for aqueous solution**
 594 **(Wexler and Clegg, 2002) accounting for the buffer capacity of the CFA samples (Experiments 1-2 in Table S1). The experiments**
 595 **conducted at around pH 2 are in red, while the experiments at around pH 3 are in black. The data uncertainty was estimated using**
 596 **the error propagation formula.**



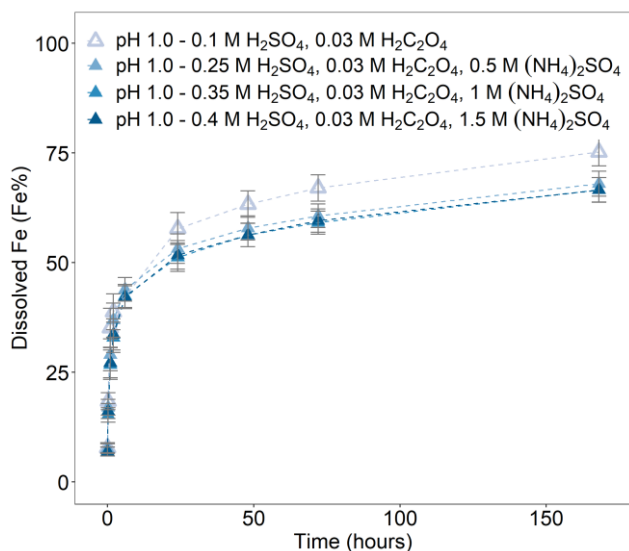
597

598 **Figure 2: Fe dissolution kinetics of a) Krakow ash, b) Aberthaw ash, and c) Shandong ash in H₂SO₄ solutions at around pH 2 (red**
 599 **open rectangles), with 0.01 M H₂C₂O₄ (red open triangles), and 1 M (NH₄)₂SO₄ (red filled triangles). The molar concentrations of**
 600 **H₂SO₄, H₂C₂O₄ and (NH₄)₂SO₄ in the experiment solutions are shown. The final pH of the experiment solutions is also reported,**
 601 **which was calculated using the E-AIM model III for aqueous solution (Wexler and Clegg, 2002) accounting for the buffer capacity**
 602 **of the CFA samples (Experiments 1, 3-4 at around pH 2). The data uncertainty was estimated using the error propagation formula.**



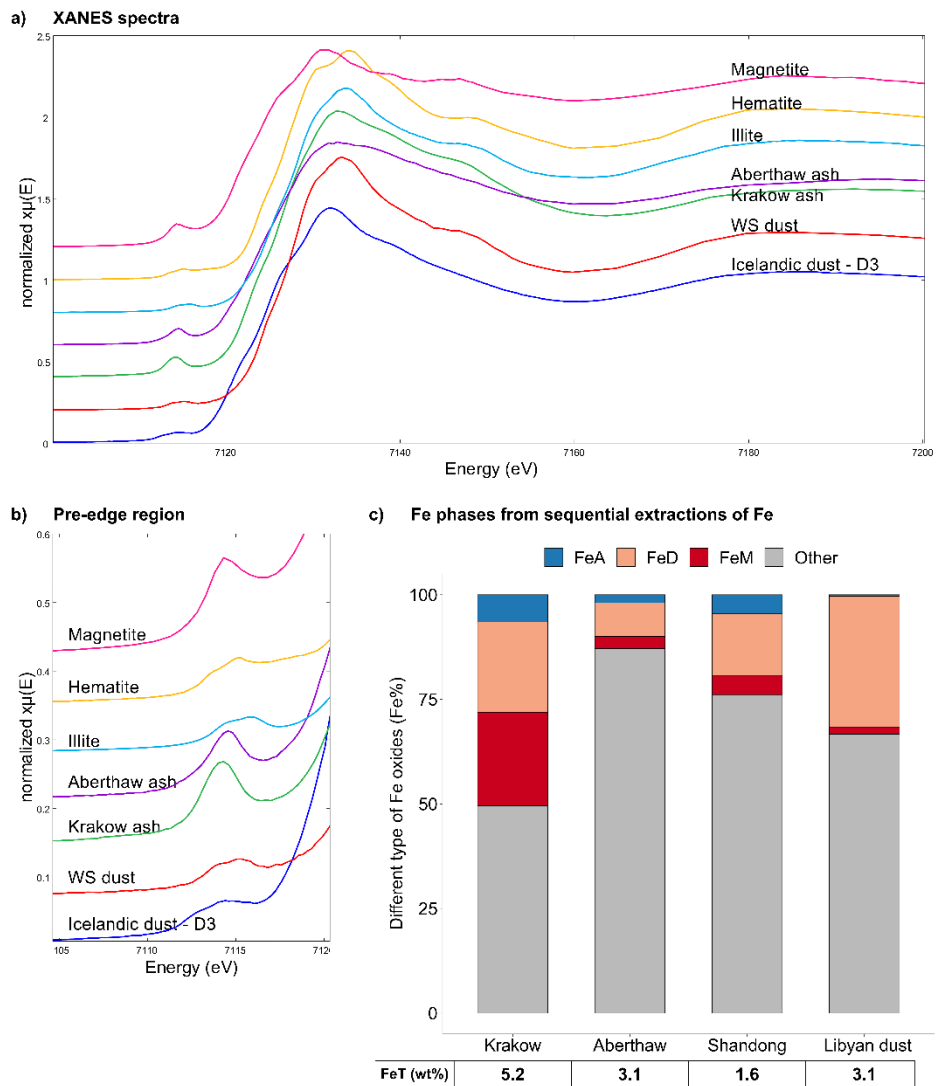
603

604 **Figure 3:** Fe dissolution kinetics of Krakow ash in H_2SO_4 solutions at pH 1.0 with 0.03 M $\text{H}_2\text{C}_2\text{O}_4$ and 1 M $(\text{NH}_4)_2\text{SO}_4$ (blue filled
 605 triangles), at pH 2.0 with 0.01 M $\text{H}_2\text{C}_2\text{O}_4$ and 1 M $(\text{NH}_4)_2\text{SO}_4$ (red filled triangles), and at pH 2.9 with 0.01 M $\text{H}_2\text{C}_2\text{O}_4$ and 1 M
 606 $(\text{NH}_4)_2\text{SO}_4$ (black filled triangles). The molar concentrations of H_2SO_4 , $\text{H}_2\text{C}_2\text{O}_4$ and $(\text{NH}_4)_2\text{SO}_4$ in the experiment solutions are shown.
 607 The final pH of the experiment solutions is also reported, which was calculated using the E-AIM model III for aqueous solution
 608 (Wexler and Clegg, 2002) accounting for the buffer capacity of the CFA samples (Experiment 7 at pH 1.0, Experiment 3 at pH 2.0,
 609 and Experiment 3 at pH 2.9 in Table S1). The data uncertainty was estimated using the error propagation formula.



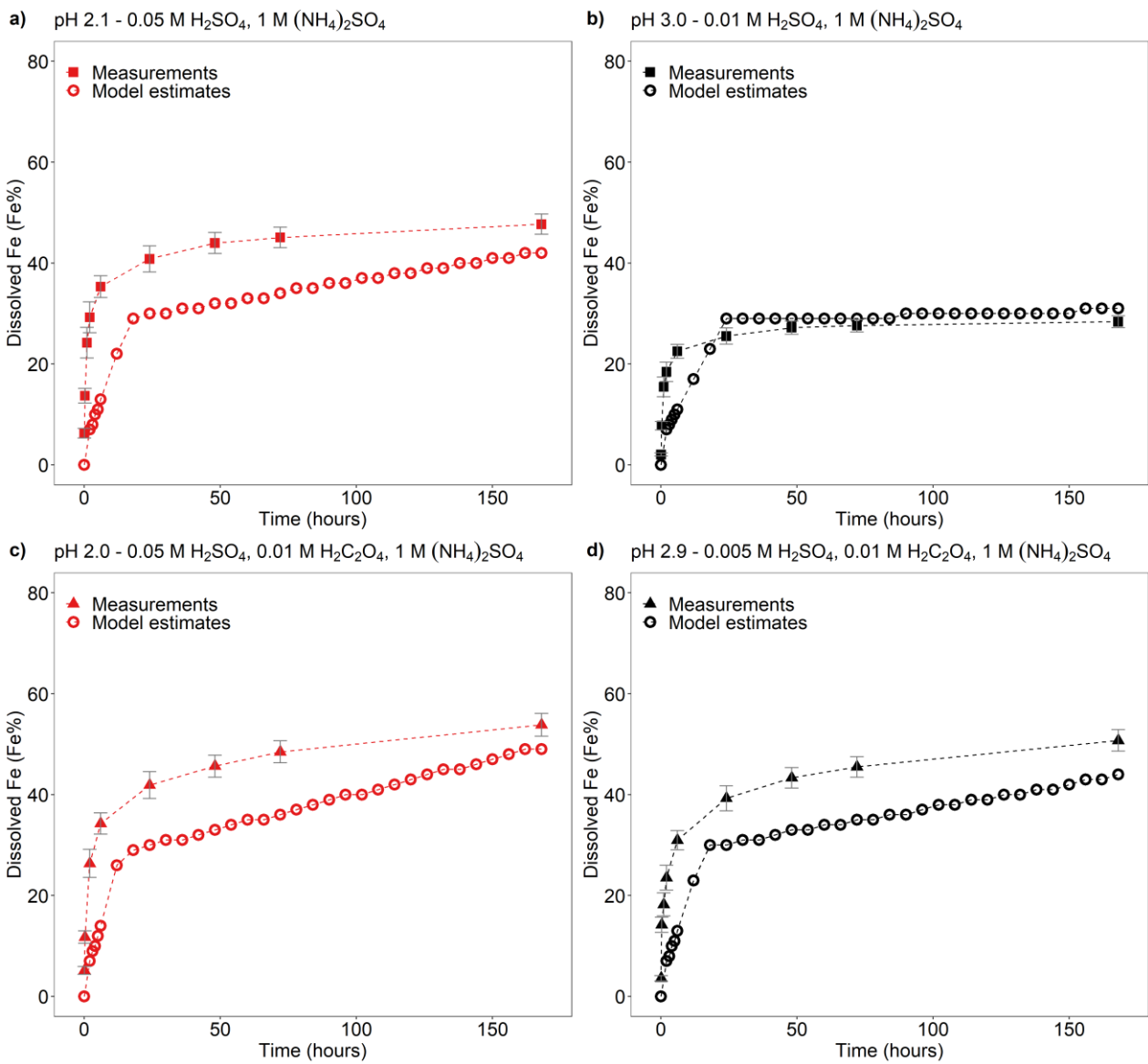
610

611 **Figure 4:** Fe dissolution kinetics of Krakow ash in H_2SO_4 solutions at pH 1.0 with 0.03 M $\text{H}_2\text{C}_2\text{O}_4$ and concentration of $(\text{NH}_4)_2\text{SO}_4$
 612 from 0 to 1.5 M. The molar concentrations of H_2SO_4 , $\text{H}_2\text{C}_2\text{O}_4$ and $(\text{NH}_4)_2\text{SO}_4$ in the experiment solutions are shown. The final pH of
 613 the experiment solutions is also reported, which was calculated using the E-AIM model III for aqueous solution (Wexler and Clegg,
 614 2002) accounting for the buffer capacity of the CFA samples (Experiments 5-8 in Table S1). The data uncertainty was estimated
 615 using the error propagation formula.



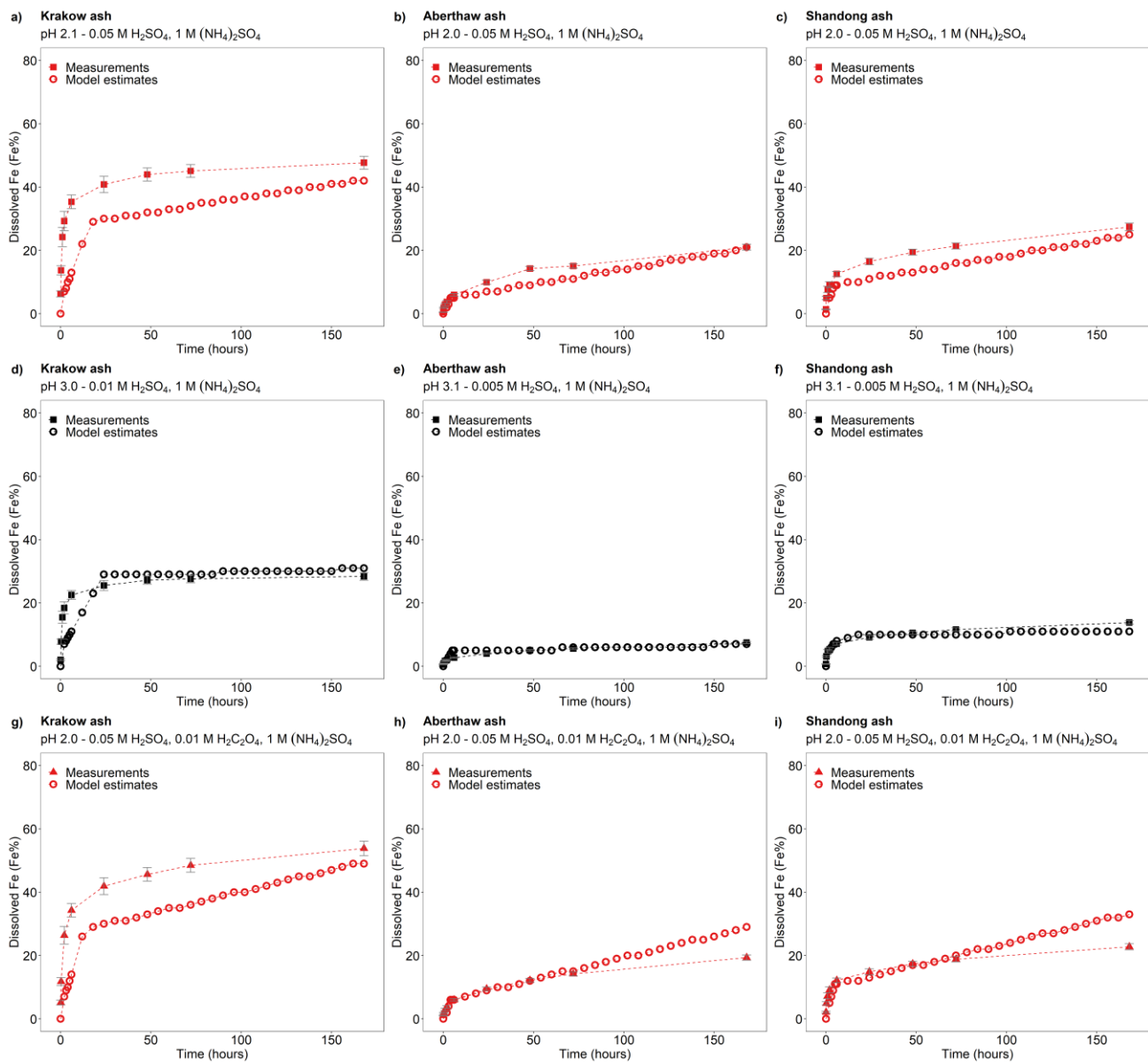
616

617 **Figure 5: Fe speciation in CFA and mineral dust samples. a-b) Fe K-edge XANES spectra of Krakow ash, Aberthaw ash, magnetite,**
 618 **hematite, and illite standards, mineral dust from the Dyngjusandur dust hotspot in Iceland - D3 (Baldo et al., 2020), and mineral**
 619 **dust from western Sahara - WS dust (Shi et al., 2011b). c) Percentages of ascorbate Fe (amorphous Fe, FeA), dithionite Fe**
 620 **(goethite/hematite, FeD), magnetite Fe (FeM), and other Fe (including Fe in aluminosilicates) to the total Fe (FeT) in the CFA**
 621 **samples and Libyan dust precursor. The FeT (as %wt.) is given below each sample column. The data uncertainty was estimated**
 622 **using the error propagation formula: 4% for FeA/FeT, 11% for FeD/FeT, 12% for FeM/FeT, and 2 % for FeT.**



623

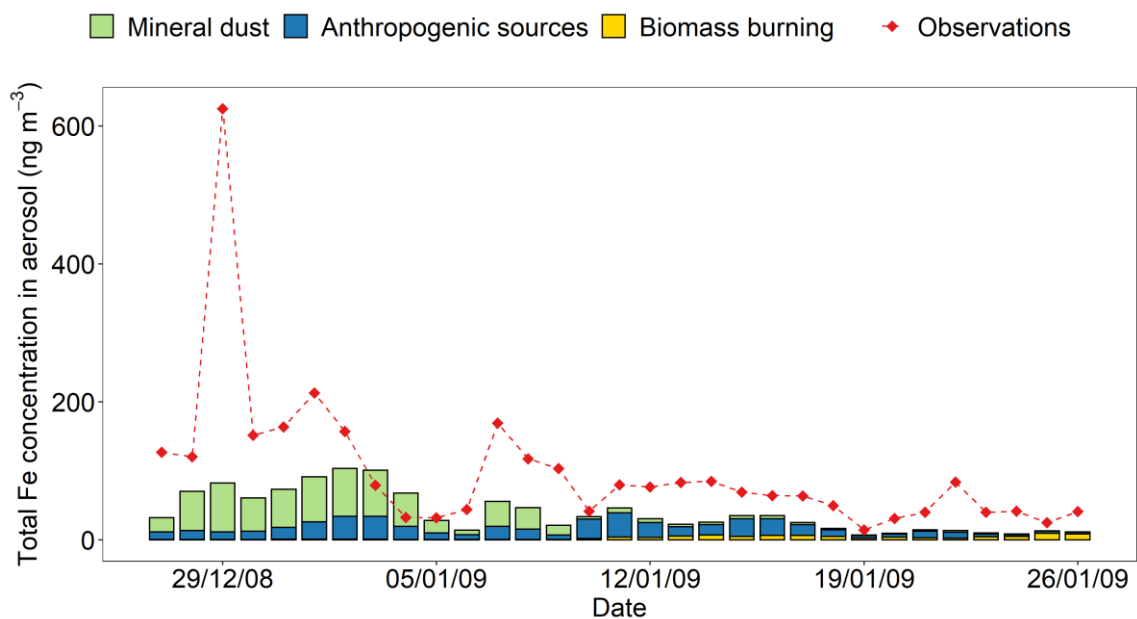
624 **Figure 6: Comparison between the Fe dissolution kinetics of Krakow ash predicted using Eq. (1) and measured in H₂SO₄ solutions**
 625 **a-b) with 1 M (NH₄)₂SO₄, c-d) with 0.01 M H₂C₂O₄ and 1 M (NH₄)₂SO₄. The molar concentrations of H₂SO₄, H₂C₂O₄ and (NH₄)₂SO₄**
 626 **in the experiment solutions are shown. The final pH of the experiment solutions is also reported, which was calculated using the E-**
 627 **AIM model III for aqueous solution (Wexler and Clegg, 2002) accounting for the buffer capacity of the CFA samples (Experiments**
 628 **2-3 in Table S1). The experiments conducted at around pH 2 are in red, while the experiments at around pH 3 are in black. The data**
 629 **uncertainty was estimated using the error propagation formula.**



630

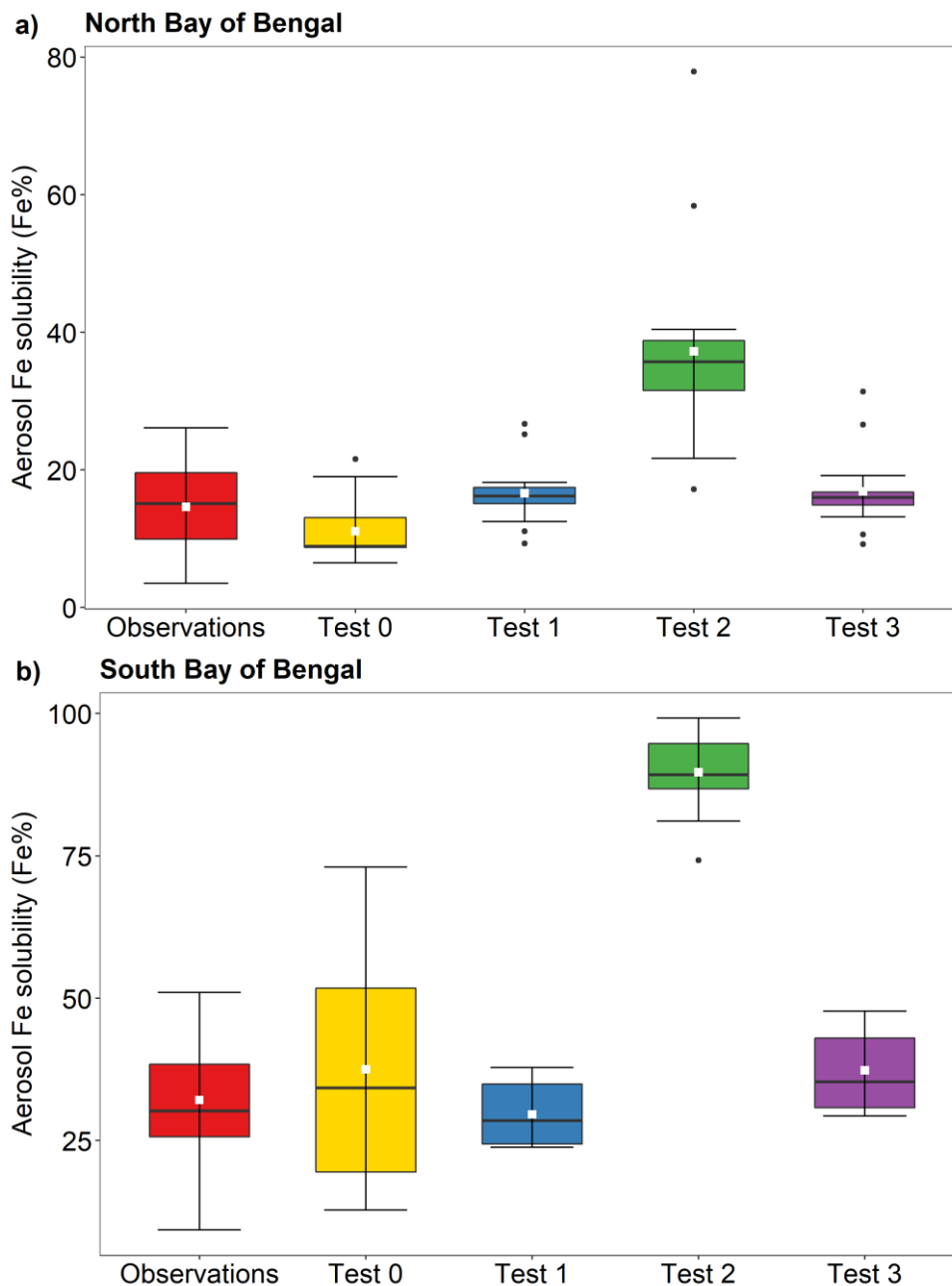
631 **Figure 7: Comparison between the Fe dissolution kinetics of Krakow, Aberthaw, and Shandong ashes predicted using Eq. (1) and**
 632 **measured in a-c) H₂SO₄ solutions at around pH 2 with 1 M (NH₄)₂SO₄ (Experiments 2 at around pH 2 in Table S1), d-f) H₂SO₄**
 633 **solutions at around pH 3 with 1 M (NH₄)₂SO₄ (Experiments 2 at around pH 3 in Table S1), g-i) H₂SO₄ solutions at pH 2.0 with 0.01**
 634 **M H₂C₂O₄ and 1 M (NH₄)₂SO₄ (Experiments 3 at pH 2.0 in Table S1). The molar concentrations of H₂SO₄, H₂C₂O₄ and (NH₄)₂SO₄**
 635 **in the experiment solutions are shown. The final pH of the experiment solutions is also reported, which was calculated using the E-**
 636 **AIM model III for aqueous solution (Wexler and Clegg, 2002) accounting for the buffer capacity of the CFA samples.**

637



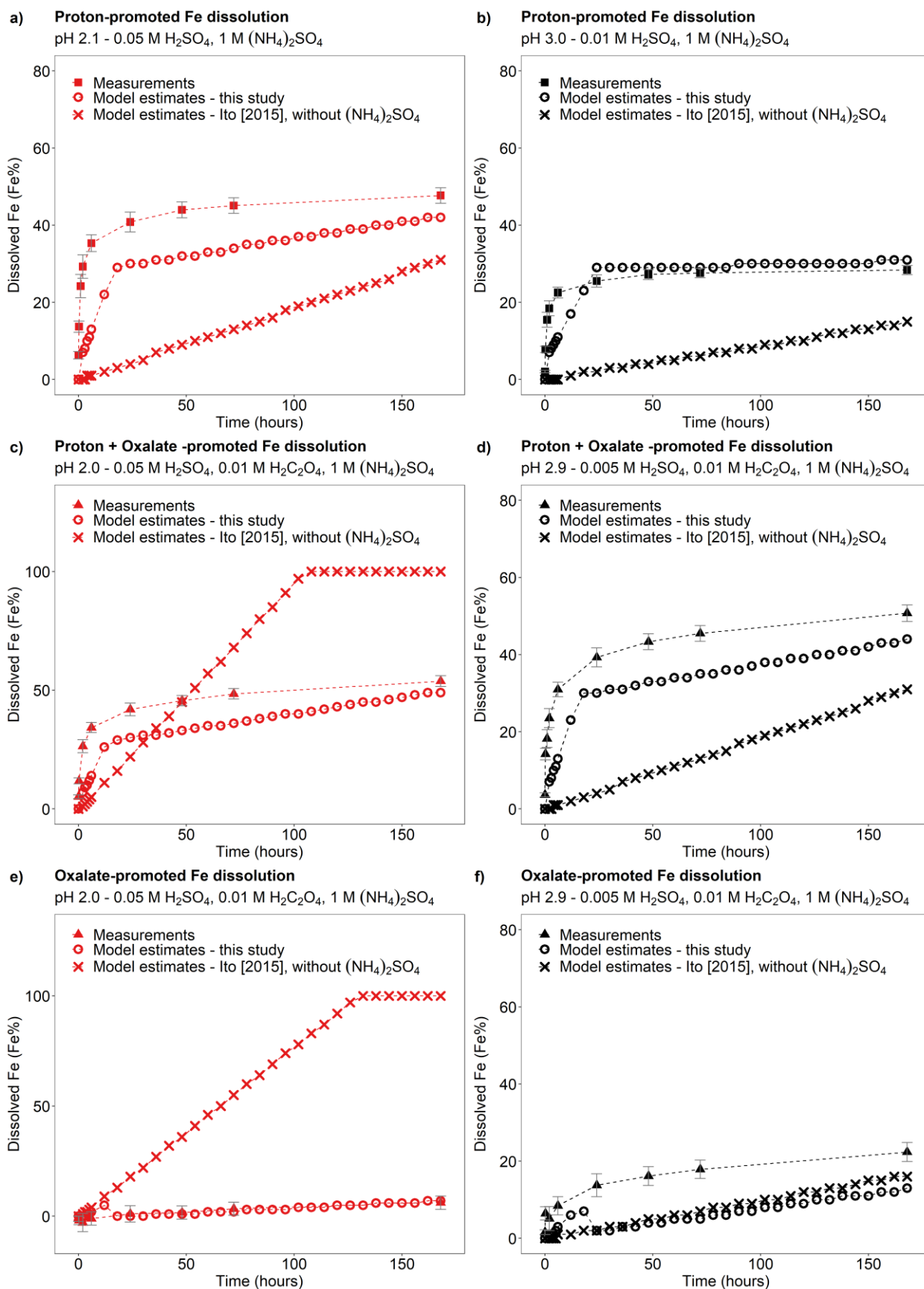
639

640 **Figure 8: Mass concentration of total Fe in PM_{2.5} aerosol particles over the Bay of Bengal from 27 December 2008 to 26 January**
 641 **2009. Observations are from Bikkina et al. (2020) (red filled diamonds). The concentrations of total Fe were calculated along the**
 642 **cruise tracks in the North Bay of Bengal (27 December 2008 - 10 January 2009) and the South Bay of Bengal (11-26 January 2009)**
 643 **using the IMPACT model. The total Fe emissions from anthropogenic combustion sources (ANTHRO) and biomass burning (BB)**
 644 **were estimated using the emission inventory of (Ito et al., 2018), whereas Fe emissions from mineral dust sources (DUST) were**
 645 **dynamically simulated (Ito et al., 2021a).**



646

647 **Figure 9:** Fe solubility in PM_{2.5} aerosol particles over a) the North Bay of Bengal, and b) the South Bay of Bengal from 27 December
 648 2008 to 26 January 2009. Observations are from Bikkina et al. (2020). Model estimates of Test 0, Test 1, Test 2, and Test 3 were
 649 calculated along the cruise tracks using the IMPACT model. In Test 0, we run the model without upgrades (Ito et al., 2021a) and
 650 applying the proton-promoted, oxalate-promoted, and photoinduced dissolution schemes for combustion aerosols in Table S6 (Ito,
 651 2015). The proton + oxalate dissolution scheme (Table 1) was applied in Test 1 and 3, while proton-promoted dissolution is used for
 652 Test 2. We adopted the base mineralogy for anthropogenic Fe emissions (Rathod et al., 2020) in Test 1 and 2. In Test 3, the Fe
 653 speciation of Krakow ash was used for all combustion sources. The small white square within the box shows the mean. The solid line
 654 within the box indicates the median. The lower and upper hinges correspond to the 25th and 75th percentiles. The whiskers above
 655 and below the box indicate the 1.5 × interquartile range, and the data outside this range are plotted individually.

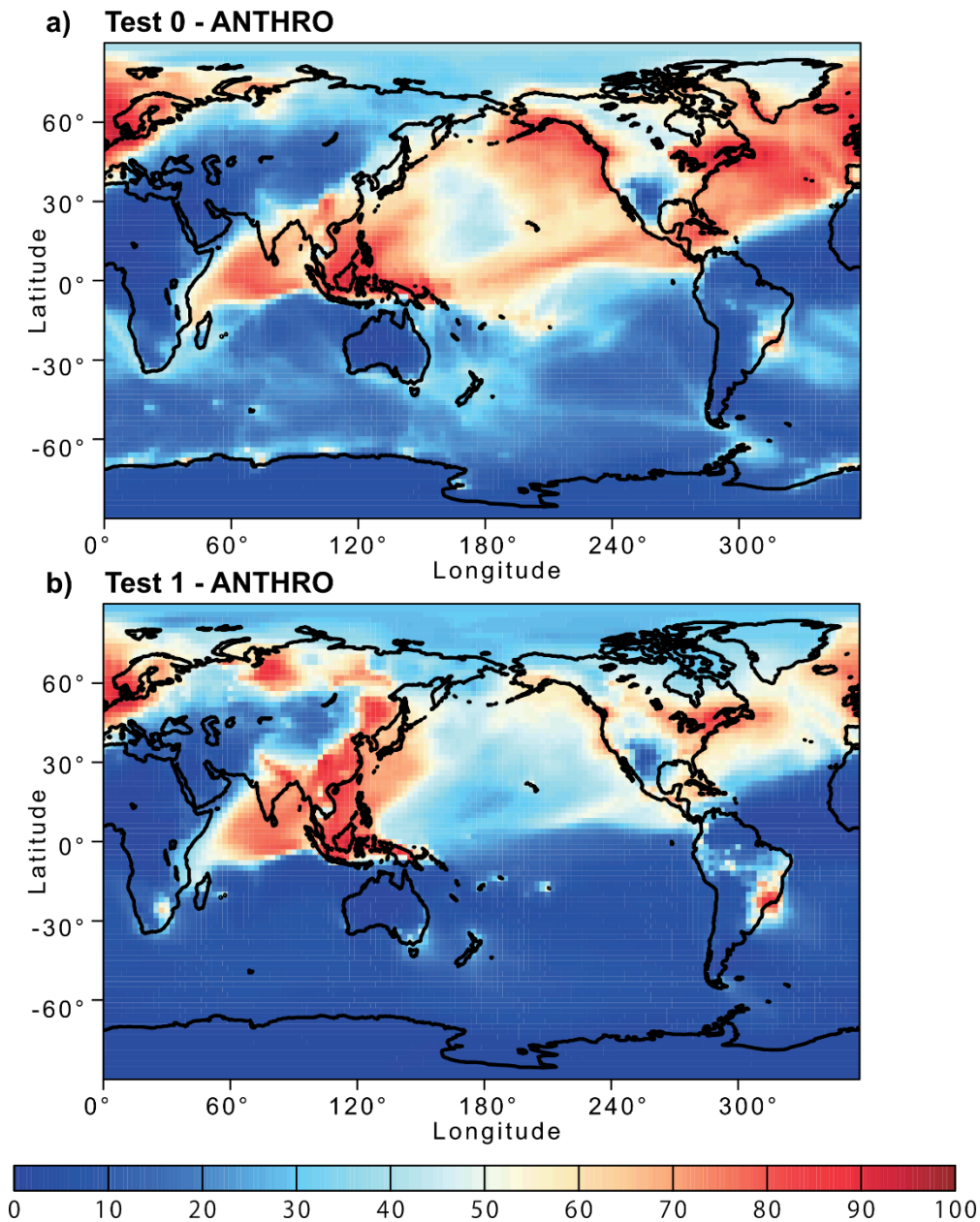


656

657 **Figure 10: Comparison between the Fe dissolution kinetics of Krakow ash calculated using the original (Ito, 2015) and the new**
 658 **dissolution scheme (Tables 1 and S6). a-b) Proton-promoted Fe dissolution in H₂SO₄ solutions with 1 M (NH₄)₂SO₄ at pH 2.1 (a),**
 659 **and at pH 3.0 (b) (Experiment 2 at pH 2.1, and Experiment 2 at pH 3.0 in Table S1). c-d) Proton + oxalate promoted Fe dissolution**
 660 **in H₂SO₄ solutions with 0.01 M H₂C₂O₄ and 1 M (NH₄)₂SO₄ at pH 2.0 (c), and at pH 2.9 (d) (Experiment 3 at pH 2.0, and Experiment**
 661 **3 at pH 2.9 in Table S1). The Fe dissolution kinetics were predicted using the rate constants in Table 1 calculated in this study (open**
 662 **circles) and the dissolution scheme for combustion aerosols in Ito (2015) (cross marks). Note that the dissolution scheme in Ito (2015)**
 663 **was calculated based on laboratory measurements conducted at low ionic strength. e-f) Contribution of the oxalate-promoted**

664 dissolution to dissolved Fe estimated using Eq. (3). The molar concentrations of H_2SO_4 , $\text{H}_2\text{C}_2\text{O}_4$ and $(\text{NH}_4)_2\text{SO}_4$ in the experiment
665 solutions are shown. The final pH of the experiment solutions is also reported, which was calculated using the E-AIM model III for
666 aqueous solution (Wexler and Clegg, 2002) accounting for the buffer capacity of the CFA samples

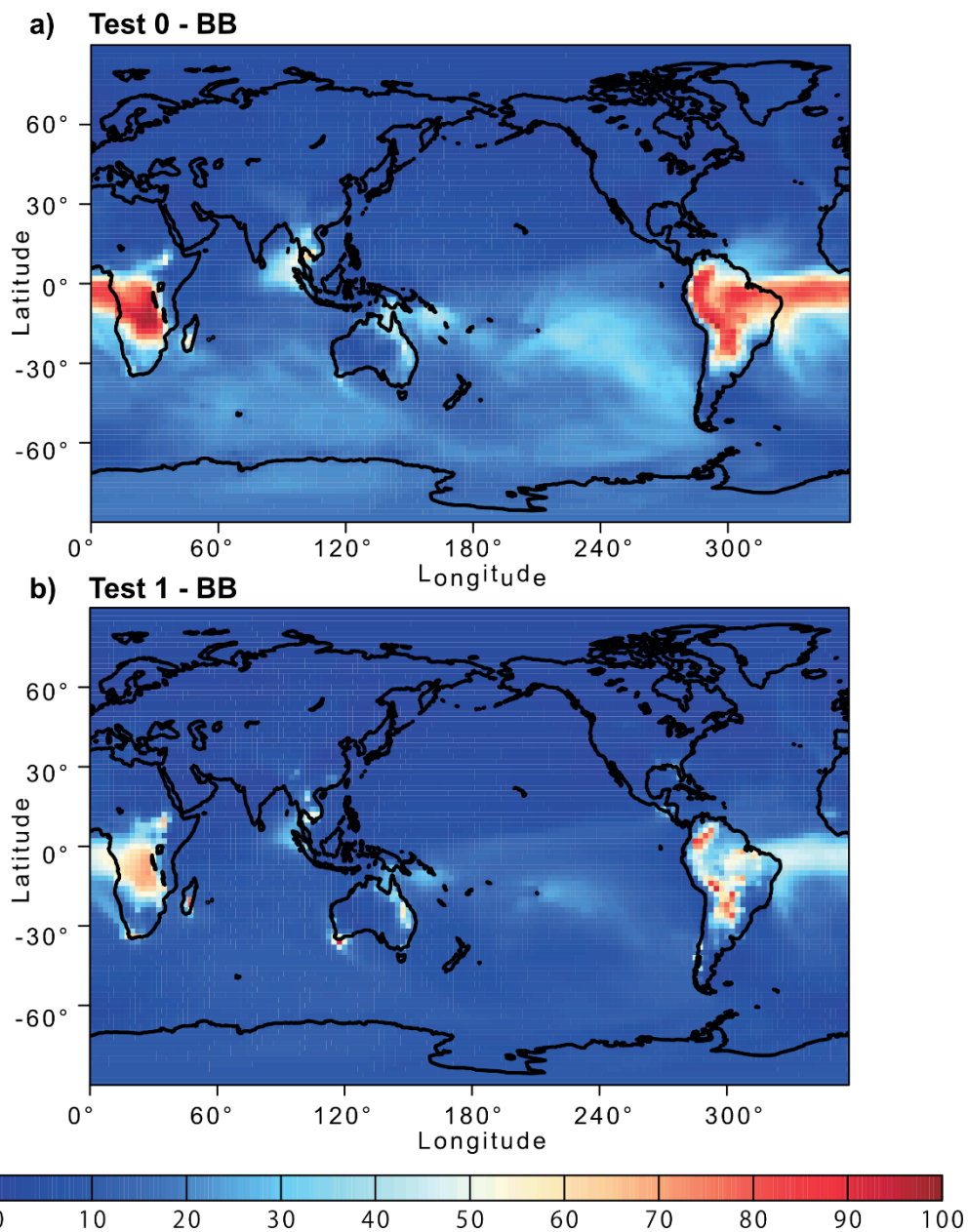
667



668

669 **Figure 11: Percentage contribution of anthropogenic combustion (ANTHRO) aerosol to the atmospheric dissolved Fe concentration**
670 **near the ground surface from a) Test 0 and b) Test 1 for December 2008 and January 2009. In Test 0, we ran the model without**
671 **upgrades in the Fe dissolution scheme (Ito et al., 2021a) and applying the proton-promoted, oxalate-promoted and photoinduced**
672 **dissolution schemes for combustion aerosols in Table S6 (Ito, 2015). The proton + oxalate dissolution scheme (Table 1) was applied**
673 **in Test 1 and we adopted the base mineralogy for anthropogenic Fe emissions (Rathod et al., 2020).**

674



675

676 **Figure 12: Percentage contribution of biomass burning (BB) aerosol to the atmospheric dissolved Fe concentration near the ground**
 677 **surface from a) Test 0 and b) Test 1 for December 2008 and January 2009. In Test 0, we ran the model without upgrades in the Fe**
 678 **dissolution scheme (Ito et al., 2021a) and applying the proton-promoted, oxalate-promoted and photoinduced dissolution schemes**
 679 **for combustion aerosols in Table S6 (Ito, 2015). The proton + oxalate dissolution scheme (Table 1) was applied in Test 1 and we**
 680 **adopted the base mineralogy for anthropogenic Fe emissions (Rathod et al., 2020).**

681

- 683 Baker, A. R., Li, M., and Chance, R.: Trace Metal Fractional Solubility in Size-Segregated Aerosols From the Tropical Eastern
684 Atlantic Ocean, *Global Biogeochem.*, 34, e2019GB006510, doi: 10.1029/2019GB006510, 2020.
- 685 Baker, A. R., Kanakidou, M., Nenes, A., Myriokefalitakis, S., Croot, P. L., Duce, R. A., Gao, Y., Guieu, C., Ito, A., Jickells,
686 T. D., Mahowald, N. M., Middag, R., Perron, M. M. G., Sarin, M. M., Shelley, R., and Turner, D. R.: Changing atmospheric
687 acidity as a modulator of nutrient deposition and ocean biogeochemistry, *Sci. Adv.*, 7, eabd8800, doi: 10.1126/sciadv.abd8800,
688 2021.
- 689 Baldo, C., Formenti, P., Nowak, S., Chevaillier, S., Cazaunau, M., Pangui, E., Di Biagio, C., Doussin, J. F., Ignatyev, K.,
690 Dagsson-Waldhauserova, P., Arnalds, O., MacKenzie, A. R., and Shi, Z.: Distinct chemical and mineralogical composition of
691 Icelandic dust compared to northern African and Asian dust, *Atmos. Chem. Phys.*, 20, 13521-13539, doi: 10.5194/acp-20-
692 13521-2020, 2020.
- 693 Bibi, I., Singh, B., and Silvester, E.: Dissolution kinetics of soil clays in sulfuric acid solutions: Ionic strength and temperature
694 effects, *Appl. Geochem.*, 51, 170-183, doi: 10.1016/j.apgeochem.2014.10.004, 2014.
- 695 Bikkina, S., Kawamura, K., Sarin, M., and Tachibana, E.: ¹³C Probing of Ambient Photo-Fenton Reactions Involving Iron and
696 Oxalic Acid: Implications for Oceanic Biogeochemistry, *ACS Earth Space Chem.*, 4, 964-976, doi:
697 10.1021/acsearthspacechem.0c00063, 2020.
- 698 Blissett, R. S., and Rowson, N. A.: A review of the multi-component utilisation of coal fly ash, *Fuel*, 97, 1-23, doi:
699 10.1016/j.fuel.2012.03.024, 2012.
- 700 Borgatta, J., Paskavitz, A., Kim, D., and Navea, J. G.: Comparative evaluation of iron leach from different sources of fly ash
701 under atmospherically relevant conditions, *Environ. Chem.*, 13, 902-912, doi: 10.1071/en16046, 2016.
- 702 Boyd, P. W., Jickells, T., Law, C. S., Blain, S., Boyle, E. A., Buesseler, K. O., Coale, K. H., Cullen, J. J., de Baar, H. J. W.,
703 Follows, M., Harvey, M., Lancelot, C., Levasseur, M., Owens, N. P. J., Pollard, R., Rivkin, R. B., Sarmiento, J., Schoemann,
704 V., Smetacek, V., Takeda, S., Tsuda, A., Turner, S., and Watson, A. J.: Mesoscale Iron Enrichment Experiments 1993-2005:
705 Synthesis and Future Directions, *Science*, 315, 612-617, doi: 10.1126/science.1131669, 2007.
- 706 British Petroleum (BP): Statistical Review of World Energy 2020, available at
707 <https://www.bp.com/en/global/corporate/energy-economics/statistical-review-of-world-energy.html>, (last access: 10 April
708 2021), 2020.
- 709 Brown, P., Jones, T., and BéruBé, K.: The internal microstructure and fibrous mineralogy of fly ash from coal-burning power
710 stations, *Environ. Pollut.*, 159, 3324-3333, doi: 10.1016/j.envpol.2011.08.041, 2011.
- 711 Chen, H., Laskin, A., Baltrusaitis, J., Gorski, C. A., Scherer, M. M., and Grassian, V. H.: Coal fly ash as a source of iron in
712 atmospheric dust, *Environ. Sci. Technol.*, 46, 2112-2120, doi: 10.1021/es204102f, 2012.
- 713 Chen, H. H., and Grassian, V. H.: Iron Dissolution of Dust Source Materials during Simulated Acidic Processing: The Effect
714 of Sulfuric, Acetic, and Oxalic Acids, *Environ. Sci. Technol.*, 47, 10312-10321, doi: 10.1021/es401285s, 2013.
- 715 Cornell, R. M., Posner, A. M., and Quirk, J. P.: Kinetics and mechanisms of the acid dissolution of goethite (α -FeOOH),
716 *Journal of Inorganic and Nuclear Chemistry*, 38, 563-567, doi: 10.1016/0022-1902(76)80305-3, 1976.
- 717 Cornell, R. M., and Schwertmann, U.: *The Iron Oxides: Structure, Properties, Reactions, Occurrence and Uses*, Wiley-VCH,
718 New York 2003.
- 719 Cwiertny, D. M., Baltrusaitis, J., Hunter, G. J., Laskin, A., Scherer, M. M., and Grassian, V. H.: Characterization and acid-
720 mobilization study of iron-containing mineral dust source materials, *J. Geophys. Res.-Atmos*, 113, D05202, doi:
721 10.1029/2007jd009332, 2008.
- 722 Dudas, M. J., and Warren, C. J.: Submicroscopic model of fly ash particles, *Geoderma*, 40, 101-114, doi: 10.1016/0016-
723 7061(87)90016-4, 1987.
- 724 Eick, M. J., Peak, J. D., and Brady, W. D.: The Effect of Oxyanions on the Oxalate-Promoted Dissolution of Goethite, *SSSAJ*,
725 63, 1133-1141, doi: doi.org/10.2136/sssaj1999.6351133x, 1999.

- 726 Emerson, E. W., Hodshire, A. L., DeBolt, H. M., Bilsback, K. R., Pierce, J. R., McMeeking, G. R., and Farmer, D. K.:
727 Revisiting particle dry deposition and its role in radiative effect estimates, *PNAS USA*, 117, 26076-26082, doi:
728 10.1073/pnas.2014761117, 2020.
- 729 Fu, H., Cwiertny, D. M., Carmichael, G. R., Scherer, M. M., and Grassian, V. H.: Photoreductive dissolution of Fe-containing
730 mineral dust particles in acidic media, *Journal of Geophysical Research*, 115, D11304, doi: 10.1029/2009jd012702, 2010.
- 731 Fu, H. B., Lin, J., Shang, G. F., Dong, W. B., Grassian, V. H., Carmichael, G. R., Li, Y., and Chen, J. M.: Solubility of Iron
732 from Combustion Source Particles in Acidic Media Linked to Iron Speciation, *Environ. Sci. Technol.*, 46, 11119-11127, doi:
733 10.1021/es302558m, 2012.
- 734 Furrer, G., and Stumm, W.: The coordination chemistry of weathering: I. Dissolution kinetics of δ -Al₂O₃ and BeO, *Geochim.*
735 *Cosmochim. Ac.*, 50, 1847-1860, doi: 10.1016/0016-7037(86)90243-7, 1986.
- 736 Hamer, M., Graham, R. C., Amrhein, C., and Bozhilov, K. N.: Dissolution of ripidolite (Mg, Fe-chlorite) in organic and
737 inorganic acid solutions, *SSSAJ*, 67, 654-661, doi: 10.2136/sssaj2003.6540, 2003.
- 738 Ito, A., and Feng, Y.: Role of dust alkalinity in acid mobilization of iron, *Atmos. Chem. Phys.*, 10, 9237-9250, doi:
739 10.5194/acp-10-9237-2010, 2010.
- 740 Ito, A.: Atmospheric Processing of Combustion Aerosols as a Source of Bioavailable Iron, *Environ. Sci. Technol. Lett.*, 2, 70-
741 75, doi: 10.1021/acs.estlett.5b00007, 2015.
- 742 Ito, A., and Shi, Z.: Delivery of anthropogenic bioavailable iron from mineral dust and combustion aerosols to the ocean,
743 *Atmos. Chem. Phys.*, 16, 85-99, doi: 10.5194/acp-16-85-2016, 2016.
- 744 Ito, A., Lin, G. X., and Penner, J. E.: Radiative forcing by light-absorbing aerosols of pyrogenetic iron oxides, *Sci. Rep.*, 8,
745 7347, doi: 10.1038/s41598-018-25756-3, 2018.
- 746 Ito, A., Myriokefalitakis, S., Kanakidou, M., Mahowald, N. M., Scanza, R. A., Hamilton, D. S., Baker, A. R., Jickells, T.,
747 Sarin, M., Bikina, S., Gao, Y., Shelley, R. U., Buck, C. S., Landing, W. M., Bowie, A. R., Perron, M. M. G., Guieu, C.,
748 Meskhidze, N., Johnson, M. S., Feng, Y., Kok, J. F., Nenes, A., and Duce, R. A.: Pyrogenic iron: The missing link to high iron
749 solubility in aerosols, *Sci. Adv.*, 5, eaau7671 doi: 10.1126/sciadv.aau7671, 2019.
- 750 Ito, A., Adebisi, A. A., Huang, Y., and Kok, J. F.: Less atmospheric radiative heating by dust due to the synergy of coarser
751 size and aspherical shape, *Atmos. Chem. Phys.*, 21, 16869–16891, doi: 10.5194/acp-21-16869-2021, 2021a.
- 752 Ito, A., Ye, Y., Baldo, C., and Shi, Z.: Ocean fertilization by pyrogenic aerosol iron, *npj Clim. Atmos. Sci.*, 4, 30, doi:
753 10.1038/s41612-021-00185-8, 2021b.
- 754 Jickells, T., and Moore, C. M.: The importance of Atmospheric Deposition for Ocean Productivity, *Annu. Rev. Ecol. Evol.*
755 *Syst.*, 46, 481-501, doi: 10.1146/annurev-ecolsys-112414-054118, 2015.
- 756 Jickells, T. D., An, Z. S., Andersen, K. K., Baker, A. R., Bergametti, G., Brooks, N., Cao, J. J., Boyd, P. W., Duce, R. A.,
757 Hunter, K. A., Kawahata, H., Kubilay, N., laRoche, J., Liss, P. S., Mahowald, N., Prospero, J. M., Ridgwell, A. J., Tegen, I.,
758 and Torres, R.: Global iron connections between desert dust, ocean biogeochemistry, and climate, *Science*, 308, 67-71, doi:
759 10.1126/science.1105959, 2005.
- 760 Johnson, M. S., and Meskhidze, N.: Atmospheric dissolved iron deposition to the global oceans: effects of oxalate-promoted
761 Fe dissolution, photochemical redox cycling, and dust mineralogy, *Geoscientific Model Development*, 6, 1137-1155, doi:
762 10.5194/gmd-6-1137-2013, 2013.
- 763 Jones, D. R.: The Leaching of Major and Trace Elements from Coal Ash, in: *Environmental Aspects of Trace Elements in*
764 *Coal*, edited by: Swaine, D. J., and Goodarzi, F., Springer Netherlands, Dordrecht, 221-262, 1995.
- 765 Kanakidou, M., Myriokefalitakis, S., and Tsigaridis, K.: Aerosols in atmospheric chemistry and biogeochemical cycles of
766 nutrients, *Environ. Res. Lett.*, 13, 063004, doi: 10.1088/1748-9326/aabcbd, 2018.
- 767 Kawamura, K., and Bikina, S.: A review of dicarboxylic acids and related compounds in atmospheric aerosols: Molecular
768 distributions, sources and transformation, *Atmos. Res.*, 170, 140-160, doi: 10.1016/j.atmosres.2015.11.018, 2016.
- 769 Kim, D., Xiao, Y., Karchere-Sun, R., Richmond, E., Ricker, H. M., Leonardi, A., and Navea, J. G.: Atmospheric Processing
770 of Anthropogenic Combustion Particles: Effects of Acid Media and Solar Flux on the Iron Mobility from Fly Ash, *ACS Earth*
771 *Space Chem.*, 4, 750-761, doi: 10.1021/acsearthspacechem.0c00057, 2020.

- 772 Kukier, U., Ishak, C. F., Sumner, M. E., and Miller, W. P.: Composition and element solubility of magnetic and non-magnetic
773 fly ash fractions, *Environ. Pollut.*, 123, 255-266, doi: 10.1016/S0269-7491(02)00376-7, 2003.
- 774 Kumar, A., Sarin, M. M., and Srinivas, B.: Aerosol iron solubility over Bay of Bengal: Role of anthropogenic sources and
775 chemical processing, *Mar. Chem.*, 121, 167-175, doi: 10.1016/j.marchem.2010.04.005, 2010.
- 776 Kutchko, B. G., and Kim, A. G.: Fly ash characterization by SEM–EDS, *Fuel*, 85, 2537-2544, doi: 10.1016/j.fuel.2006.05.016,
777 2006.
- 778 Lawson, M. J., Prytherch, Z. C., Jones, T. P., Adams, R. A., and BéruBé, K. A.: Iron-Rich Magnetic Coal Fly Ash Particles
779 Induce Apoptosis in Human Bronchial Cells, *Appl. Sci.*, 10, 8368, doi: 10.3390/app10238368, 2020.
- 780 Lee, S. O., Tran, T., Jung, B. H., Kim, S. J., and Kim, M. J.: Dissolution of iron oxide using oxalic acid, *Hydrometallurgy*, 87,
781 91-99, doi: 10.1016/j.hydromet.2007.02.005, 2007.
- 782 Li, J., Anderson, J. R., and Buseck, P. R.: TEM study of aerosol particles from clean and polluted marine boundary layers over
783 the North Atlantic, *J. Geophys. Res.-Atmos*, 108, doi: 10.1029/2002JD002106, 2003.
- 784 Li, W. J., Xu, L., Liu, X. H., Zhang, J. C., Lin, Y. T., Yao, X. H., Gao, H. W., Zhang, D. Z., Chen, J. M., Wang, W. X.,
785 Harrison, R. M., Zhang, X. Y., Shao, L. Y., Fu, P. Q., Nenes, A., and Shi, Z. B.: Air pollution-aerosol interactions produce
786 more bioavailable iron for ocean ecosystems, *Sci. Adv.*, 3, e1601749, doi: 10.1126/sciadv.1601749, 2017.
- 787 Mahowald, N. M., Kloster, S., Engelstaedter, S., Moore, J. K., Mukhopadhyay, S., McConnell, J. R., Albani, S., Doney, S. C.,
788 Bhattacharya, A., Curran, M. A. J., Flanner, M. G., Hoffman, F. M., Lawrence, D. M., Lindsay, K., Mayewski, P. A., Neff, J.,
789 Rothenberg, D., Thomas, E., Thornton, P. E., and Zender, C. S.: Observed 20th century desert dust variability: impact on
790 climate and biogeochemistry, *Atmos. Chem. Phys.*, 10, 10875-10893, doi: 10.5194/acp-10-10875-2010, 2010.
- 791 Marcotte, A. R., Anbar, A. D., Majestic, B. J., and Herckes, P.: Mineral Dust and Iron Solubility: Effects of Composition,
792 Particle Size, and Surface Area, *Atmosphere*, 11, 533, doi: 10.3390/atmos11050533, 2020.
- 793 Martin, J. H.: Glacial-interglacial CO₂ change: The Iron Hypothesis, *Paleoceanography*, 5, 1-13, doi:
794 10.1029/PA005i001p000001, 1990.
- 795 Matsuo, M., Kobayashi, T., Singh, T. B., Tsurumi, M., and Ichikuni, M.: ⁵⁷Fe Mössbauer spectroscopic study of Japanese
796 cedar bark — The variation in chemical states of iron due to influence of human activities, *Hyperfine Interact.*, 71, 1255-1258,
797 doi: 10.1007/BF02397311, 1992.
- 798 Meskhidze, N., Chameides, W. L., Nenes, A., and Chen, G.: Iron mobilization in mineral dust: Can anthropogenic SO₂
799 emissions affect ocean productivity?, *Geophys. Res. Lett.*, 30, 2085, doi: 10.1029/2003gl018035, 2003.
- 800 Mills, M. M., Ridame, C., Davey, M., La Roche, J., and Geider, R. J.: Iron and phosphorus co-limit nitrogen fixation in the
801 eastern tropical North Atlantic, *Nature*, 429, 292-294, doi: 10.1038/nature02550, 2004.
- 802 Moore, C. M., Mills, M. M., Milne, A., Langlois, R., Achterberg, E. P., Lochte, K., Geider, R. J., and La Roche, J.: Iron limits
803 primary productivity during spring bloom development in the central North Atlantic, *Glob. Change Biol.*, 12, 626-634, doi:
804 10.1111/j.1365-2486.2006.01122.x, 2006.
- 805 Munawar, M. E.: Human health and environmental impacts of coal combustion and post-combustion wastes, *J. Sustain. Min.*,
806 17, 87-96, doi: 10.1016/j.jsm.2017.12.007, 2018.
- 807 Paris, R., Desboeufs, K. V., and Journet, E.: Variability of dust iron solubility in atmospheric waters: Investigation of the role
808 of oxalate organic complexation, *Atmos. Environ.*, 45, 6510-6517, doi: 10.1016/j.atmosenv.2011.08.068, 2011.
- 809 Paris, R., and Desboeufs, K. V.: Effect of atmospheric organic complexation on iron-bearing dust solubility, *Atmos. Chem.*
810 *Phys.*, 13, 4895-4905, doi: 10.5194/acp-13-4895-2013, 2013.
- 811 Poulton, S. W., and Canfield, D. E.: Development of a sequential extraction procedure for iron: implications for iron
812 partitioning in continentally derived particulates, *Chem. Geol.*, 214, 209-221, doi: 10.1016/j.chemgeo.2004.09.003, 2005.
- 813 Pye, H. O. T., Nenes, A., Alexander, B., Ault, A. P., Barth, M. C., Clegg, S. L., Collett Jr, J. L., Fahey, K. M., Hennigan, C.
814 J., Herrmann, H., Kanakidou, M., Kelly, J. T., Ku, I. T., McNeill, V. F., Riemer, N., Schaefer, T., Shi, G., Tilgner, A., Walker,
815 J. T., Wang, T., Weber, R., Xing, J., Zaveri, R. A., and Zuend, A.: The acidity of atmospheric particles and clouds, *Atmos.*
816 *Chem. Phys.*, 20, 4809-4888, doi: 10.5194/acp-20-4809-2020, 2020.

- 817 Raiswell, R., Benning, L. G., Tranter, M., and Tulaczyk, S.: Bioavailable iron in the Southern Ocean: the significance of the
818 iceberg conveyor belt, *Geochemical Transactions*, 9, doi: 10.1186/1467-4866-9-7, 2008.
- 819 Rathod, S. D., Hamilton, D. S., Mahowald, N. M., Klimont, Z., Corbett, J. J., and Bond, T. C.: A Mineralogy - Based
820 Anthropogenic Combustion - Iron Emission Inventory, *J. Geophys. Res.-Atmos*, 125, e2019JD032114, doi:
821 10.1029/2019jd032114, 2020.
- 822 Ravel, B., and Newville, M.: ATHENA, ARTEMIS, HEPHAESTUS: data analysis for X-ray absorption spectroscopy using
823 IFEFFIT, *J. Synchrotron Radiat.*, 12, 537-541, doi: 10.1107/S0909049505012719, 2005.
- 824 Rubasinghege, G., Lentz, R. W., Scherer, M. M., and Grassian, V. H.: Simulated atmospheric processing of iron oxyhydroxide
825 minerals at low pH: roles of particle size and acid anion in iron dissolution, *PNAS USA*, 107, 6628-6633, doi:
826 10.1073/pnas.0910809107, 2010.
- 827 Rubin, M., Berman-Frank, I., and Shaked, Y.: Dust- and mineral-iron utilization by the marine dinitrogen-fixer *Trichodesmium*,
828 *Nat. Geosci.*, 4, 529-534, doi: 10.1038/ngeo1181, 2011.
- 829 Schlosser, C., Schmidt, K., Aquilina, A., Homoky, W. B., Castrillejo, M., Mills, R. A., Patey, M. D., Fielding, S., Atkinson,
830 A., and Achterberg, E. P.: Mechanisms of dissolved and labile particulate iron supply to shelf waters and phytoplankton blooms
831 off South Georgia, Southern Ocean, *Biogeosciences*, 15, 4973-4993, doi: 10.5194/bg-15-4973-2018, 2018.
- 832 Schwertmann, U.: Solubility and dissolution of iron oxides, *Plant Soil*, 130, 1-25, doi: 10.1007/BF00011851, 1991.
- 833 Seinfeld, J. H., and Pandis, S. N.: Atmospheric chemistry and physics: from air pollution to climate change, John Wiley &
834 Sons, 2016.
- 835 Shelley, R. U., Landing, W. M., Ussher, S. J., Planquette, H., and Sarthou, G.: Regional trends in the fractional solubility of
836 Fe and other metals from North Atlantic aerosols (GEOTRACES cruises GA01 and GA03) following a two-stage leach,
837 *Biogeosciences*, 15, 2271-2288, doi: 10.5194/bg-15-2271-2018, 2018.
- 838 Shi, Z., Krom, M. D., Bonneville, S., Baker, A. R., Jickells, T. D., and Benning, L. G.: Formation of iron nanoparticles and
839 increase in iron reactivity in the mineral dust during simulated cloud processing, *Environ. Sci. Technol.*, 43, 6592-6596, doi:
840 10.1021/es901294g, 2009.
- 841 Shi, Z., Bonneville, S., Krom, M. D., Carslaw, K. S., Jickells, T. D., Baker, A. R., and Benning, L. G.: Iron dissolution kinetics
842 of mineral dust at low pH during simulated atmospheric processing, *Atmos. Chem. Phys.*, 11, 995-1007, doi: 10.5194/acp-11-
843 995-2011, 2011a.
- 844 Shi, Z., Krom, M. D., Bonneville, S., Baker, A. R., Bristow, C., Drake, N., Mann, G., Carslaw, K., McQuaid, J. B., Jickells,
845 T., and Benning, L. G.: Influence of chemical weathering and aging of iron oxides on the potential iron solubility of Saharan
846 dust during simulated atmospheric processing, *Global Biogeochem.*, 25, GB2010, doi: 10.1029/2010gb003837, 2011b.
- 847 Shi, Z., Krom, M. D., Jickells, T. D., Bonneville, S., Carslaw, K. S., Mihalopoulos, N., Baker, A. R., and Benning, L. G.:
848 Impacts on iron solubility in the mineral dust by processes in the source region and the atmosphere: A review, *Aeolian Res.*,
849 5, 21-42, doi: 10.1016/j.aeolia.2012.03.001, 2012.
- 850 Shi, Z., Krom, M. D., Bonneville, S., and Benning, L. G.: Atmospheric processing outside clouds increases soluble iron in
851 mineral dust, *Environ. Sci. Technol.*, 49, 1472-1477, doi: 10.1021/es504623x, 2015.
- 852 Shi, Z. B., Woodhouse, M. T., Carslaw, K. S., Krom, M. D., Mann, G. W., Baker, A. R., Savov, I., Fones, G. R., Brooks, B.,
853 Drake, N., Jickells, T. D., and Benning, L. G.: Minor effect of physical size sorting on iron solubility of transported mineral
854 dust, *Atmos. Chem. Phys.*, 11, 8459-8469, doi: 10.5194/acp-11-8459-2011, 2011c.
- 855 Sholkovitz, E. R., Sedwick, P. N., and Church, T. M.: Influence of anthropogenic combustion emissions on the deposition of
856 soluble aerosol iron to the ocean: Empirical estimates for island sites in the North Atlantic, *Geochim. Cosmochim. Ac.*, 73,
857 3981-4003, doi: 10.1016/j.gca.2009.04.029, 2009.
- 858 Sholkovitz, E. R., Sedwick, P. N., Church, T. M., Baker, A. R., and Powell, C. F.: Fractional solubility of aerosol iron:
859 Synthesis of a global-scale data set, *Geochim. Cosmochim. Ac.*, 89, 173-189, doi: 10.1016/j.gca.2012.04.022, 2012.
- 860 Sidhu, P. S., Gilkes, R. J., Cornell, R. M., Posner, A. M., and Quirk, J. P.: Dissolution of Iron Oxides and Oxyhydroxides in
861 Hydrochloric and Perchloric Acids, *Clays Clay Miner.*, 29, 269-276, doi: 10.1346/CCMN.1981.0290404, 1981.

- 862 Spokes, L. J., and Jickells, T. D.: Factors controlling the solubility of aerosol trace metals in the atmosphere and on mixing
863 into seawater, *Aquat. Geochem.*, 1, 355-374, doi: 10.1007/BF00702739, 1995.
- 864 Srinivas, B., Sarin, M. M., and Kumar, A.: Impact of anthropogenic sources on aerosol iron solubility over the Bay of Bengal
865 and the Arabian Sea, *Biogeochemistry*, 110, 257-268, doi: 10.1007/s10533-011-9680-1, 2012.
- 866 Srinivas, B., and Sarin, M. M.: Atmospheric dry-deposition of mineral dust and anthropogenic trace metals to the Bay of
867 Bengal, *J. Mar. Syst.*, 126, 56-68, doi: 10.1016/j.jmarsys.2012.11.004, 2013.
- 868 Surana, V., and Warren, I.: The leaching of goethite, *Transactions of the Institute of Mining and Metallurgy*, 80, C152-155,
869 1969.
- 870 Sutto, T. E.: Magnetite fine particle and nanoparticle environmental contamination from industrial uses of coal, *Environ. Pollut.*,
871 243, 528-533, doi: 10.1016/j.envpol.2018.08.080, 2018.
- 872 Valeev, D., Mikhailova, A., and Atmadzhidi, A.: Kinetics of Iron Extraction from Coal Fly Ash by Hydrochloric Acid
873 Leaching, *Metals*, 8, 533, doi: 10.3390/met8070533, 2018.
- 874 Valeev, D., Kunilova, I., Alpatov, A., Varnavskaya, A., and Ju, D.: Magnetite and Carbon Extraction from Coal Fly Ash Using
875 Magnetic Separation and Flotation Methods, *Minerals*, 9, 320, doi: 10.3390/min9050320, 2019.
- 876 Viollier, E., Inglett, P. W., Hunter, K., Roychoudhury, A. N., and Van Cappellen, P.: The ferrozine method revisited:
877 Fe(II)/Fe(III) determination in natural waters, *Appl. Geochem.*, 15, 785-790, doi: 10.1016/s0883-2927(99)00097-9, 2000.
- 878 Waanders, F. B., Vinken, E., Mans, A., and Mulaba-Bafubiandi, A. F.: Iron Minerals in Coal, Weathered Coal and Coal Ash
879 – SEM and Mössbauer Results, *Hyperfine Interact.*, 148, 21-29, doi: 10.1023/B:HYPE.0000003760.89706.f6, 2003.
- 880 Wang, R., Balkanski, Y., Boucher, O., Bopp, L., Chappell, A., Ciais, P., Hauglustaine, D., Penuelas, J., and Tao, S.: Sources,
881 transport and deposition of iron in the global atmosphere, *Atmos. Chem. Phys.*, 15, 6247-6270, doi: 10.5194/acp-15-6247-
882 2015, 2015.
- 883 Wang, X. S.: Mineralogical and chemical composition of magnetic fly ash fraction, *Environ. Earth Sci.*, 71, 1673-1681, doi:
884 10.1007/s12665-013-2571-0, 2014.
- 885 Warren, C. J., and Dudas, M. J.: Leachability and partitioning of elements in ferromagnetic fly ash particles, *Sci. Total Environ.*,
886 84, 223-236, doi: 10.1016/0048-9697(89)90385-9, 1989.
- 887 Wexler, A. S., and Clegg, S. L.: Atmospheric aerosol models for systems including the ions H^+ , NH_4^+ , Na^+ , SO_4^{2-} , NO_3^- , Cl^- ,
888 Br^- , and H_2O , *J. Geophys. Res.-Atmos.*, 107, 4207, doi: 10.1029/2001JD000451, 2002.
- 889 Xu, N., and Gao, Y.: Characterization of hematite dissolution affected by oxalate coating, kinetics and pH, *Appl. Geochem.*,
890 23, 783-793, doi: 10.1016/j.apgeochem.2007.12.026, 2008.
- 891 Yao, Z. T., Ji, X. S., Sarker, P. K., Tang, J. H., Ge, L. Q., Xia, M. S., and Xi, Y. Q.: A comprehensive review on the applications
892 of coal fly ash, *Earth-Sci. Rev.*, 141, 105-121, doi: 10.1016/j.earscirev.2014.11.016, 2015.
- 893 Yu, J. Z., Huang, X.-F., Xu, J., and Hu, M.: When Aerosol Sulfate Goes Up, So Does Oxalate: Implication for the Formation
894 Mechanisms of Oxalate, *Environ. Sci. Technol.*, 39, 128-133, doi: 10.1021/es049559f, 2005.
- 895 Zhang, D., Iwasaka, Y., Shi, G., Zang, J., Matsuki, A., and Trochkin, D.: Mixture state and size of Asian dust particles
896 collected at southwestern Japan in spring 2000, *J. Geophys. Res.-Atmos.*, 108, 4760, doi: 10.1029/2003JD003869, 2003.
- 897 Zhao, Y., Zhang, J., Sun, J., Bai, X., and Zheng, C.: Mineralogy, Chemical Composition, and Microstructure of Ferrospheres
898 in Fly Ashes from Coal Combustion, *Energy Fuels*, 20, 1490-1497, doi: 10.1021/ef060008f, 2006.
- 899 Zhu, X. R., Prospero, J. M., Millero, F. J., Savoie, D. L., and Brass, G. W.: The solubility of ferric ion in marine mineral
900 aerosol solutions at ambient relative humidities *Mar. Chem.*, 38, 91-107, doi: 10.1016/0304-4203(92)90069-m, 1992.

901